8-20-2012 12:00 AM

Numerical Simulation of Catalytic Ozone Decomposition Reaction in a Gas-solids Circulating Fluidized Bed Riser

Lei Kong
The University of Western Ontario

Supervisor
Prof. Chao Zhang
The University of Western Ontario Joint Supervisor
Prof. Jesse Zhu
The University of Western Ontario

Graduate Program in Mechanical and Materials Engineering
A thesis submitted in partial fulfillment of the requirements for the degree in Master of Engineering Science

NUMERICAL SIMULATIONS OF CATALYTIC OZONE DECOMPOSITION REACTION IN A GAS-SOLIDS CIRCULATING FLUIDIZED BED RISER
(Spine title: NUMERICAL SIMULATIONS OF CATALYTIC OZONE DECOMPOSITION REACTION IN CFB RISER)
(Thesis format: Integrated Article)

by

Lei Kong

Graduate Program in Mechanical and Materials Engineering

A thesis submitted in partial fulfillment
of the requirements for the degree of
Master of Engineering Science

The School of Graduate and Postdoctoral Studies
The University of Western Ontario
London, Ontario, Canada

THE UNIVERSITY OF WESTERN ONTARIO
SCHOOL OF GRADUATE AND POSTDOCTORAL STUDIES

CERTIFICATE OF EXAMINATION

Supervisors

Prof. Chao Zhang

Prof. Jesse Zhu

Co-Supervisor

Supervisory Committee

Prof. Roger E. Khayat

Examiners

Prof. Roger E. Khayat

Prof. Eric Savory

Prof. Madhumita B. Ray

The thesis by

Lei Kong

entitled:

Numerical Simulation of Catalytic Ozone Decomposition Reaction in a Gas-solids Circulating Fluidized Bed Riser

is accepted in partial fulfillment of the
requirements for the degree of
Master of Engineering Science

Date_____

Chair of the Thesis Examination Board

Abstract

Computational fluid dynamics (CFD) modeling of catalytic ozone decomposition reaction in a circulating fluidized bed (CFB) riser using iron impregnated FCC particles as catalyst is carried out. The catalytic reaction is defined as a one-step reaction with an empirical coefficient. Eularian-Eularian method with kinetic theory of granular flow is used to solve the gas-solids two-phase flow in the CFB riser. The simulation results are compared with experimental data, with the reaction rate modified using an empirical coefficient to provide better simulation results than the original reaction rate. Moreover, the particle size has great effects on the reaction rate. Studies on solid particle distribution show that the influence of wall boundary condition, determined by specularity coefficient and particle-wall restitution coefficient, plays a major role in the solids lateral velocity that affects the solids distribution in the riser. The generality of the CFD model is further validated under different operating conditions of the riser.

Keywords: numerical simulation, computational fluid dynamics (CFD), circulating fluidized bed (CFB) risers, gas-solids two-phase flow, catalytic ozone decomposition reaction, specularity coefficient, particle-wall restitution coefficient

Co-authorship

Chapter 3: Evaluation of the effect of wall boundary conditions on numerical simulations of circulating fluidized beds

Authors: Lei Kong; Chao Zhang; Jesse Zhu

Lei Kong carried out the numerical simulations and data analyses under the guidance of Dr. J. Zhu and Dr. C. Zhang. The draft of manuscript was written by Lei Kong. Revisions were carried out under the close supervision of Dr. J. Zhu and Dr. C. Zhang. The final version is ready for submission.

Chapter 4: Two dimensional simulation of catalytic ozone decomposition reaction in a gas-solids circulating fluidized bed riser

Authors: Lei Kong; Chao Zhang; Jesse Zhu

Lei Kong carried out the numerical simulations and data analyses under the guidance of Dr. J. Zhu and Dr. C. Zhang. The draft of manuscript was written by Lei Kong. Revisions were carried out under the close supervision of Dr. J. Zhu and Dr. C. Zhang. The final version has been submitted to the journal, Industry & Engineering Chemistry Research.

Acknowledgment

First, I would like to offer my sincerest gratitude to Profs. Zhang and Zhu, who have supported me throughout my research with their knowledge and patience. I attribute the thesis to their encouragements and efforts and without them it would not have been completed. One simply could not wish for better or friendlier supervisors.

Then I would like to thank all the members of research groups of Profs. Zhang and Zhu, especially Rajeev Kumar, Abbas Dadashi, Rajib Kumar Saha and Chengxiu Wang for their help and advices.

Finally, I would like to thank to Huixu, Xiang and my parents for their moral supports throughout the entire process.

Table of Contents

List of figures

List of tables

Chapter 1.

1 Introduction

In this study, a computational fluid dynamics (CFD) model has been developed to simulate catalytic ozone decomposition reaction in a gas-solids circulating fluidized bed (CFB) riser. The introduction of the research background, literature review, objectives and thesis structure are presented in this chapter.

1.1 Background

Fluidization is a process that fine solid particles are transformed from a fixed solid-like state into a fluid-like state through contacting with a moving fluid, either a gas or a liquid. When a fluid is injected from the bottom of a bed of solid particles, it will flow upwards through the bed of particles via the space between the particles. When the velocity of the fluid is low, the drag force on particles is also low, and thus the bed remains in a fixed state. When the fluid velocity is increased, the drag force will begin to counteract the gravity, causing the bed to expand in volume as the particles move away from each other. Further increasing the fluid velocity, there will be a critical value at which the upward drag force will exactly equal to the gravitational force, so the particles become suspended within the fluid. At this critical value, the bed is considered as being fluidized and will exhibit fluid-like behaviour. Further increasing the fluid velocity, the bulk density of the bed will keep decreasing, and the fluidization becomes more intense, until the particles no longer form as a bed and are entrained upwards by the fluid flow.

A gas-solids fluidized bed is a reactor device based on the fluidization phenomenon between gas and solid particles, which can be applied to implement a variety of multiphase chemical reactions. In a gas-solids fluidized bed, gas is introduced through granular solid particles at a velocity high enough to fluidize the particles to make it flow as a fluid. Depending on the magnitude of the fluid velocity, when it is increased, there will be bubbling fluidization, slugging fluidization, turbulent fluidization, circulating fluidization and dilute phase conveying regimes. A fluidization operated under high gas velocity in the circulating flow regime is a CFB, which is the subject of the study here.

The industrial purpose of CFB applications can be traced back to the 1940s when fluid catalytic cracking (FCC) technology was first developed (Zhu and Cheng 2005). However, as a result of low catalyst activity and other technical problems, it was not used until in the 1970s when the concept of circulating fluidization was first reported (Yerushalmi, Turner, and Squires 1976).

There is a considerable progress of the research on CFB reactors. Many researchers have confirmed the remarkable features of CFBs, such as higher gas-solids contact efficiency, reduced axial dispersion for both gas and solids phases and higher gas-solids throughput. Thus, CFBs have been used in various chemical processes, including FCC, combustion of low grade coal, fluid hydroforming etc. (Grace 1990; Reh 1999; Zhu and Cheng 2005).

The aerodynamic study is important in improving CFB designs. A non-uniform radial distribution of the solid particles was detected, which is called core-annulus structure

(Qi et al. 2003; Yan and Zhu 2004; Huang, Zhu, and Parssinen 2006; Huang, Yan, and Zhu 2007; Miller and Gidaspow 1992; Li 2010). Core-annulus structure of solid particles in the radial profile represents a dense solids region near the wall and a dilute solids region in the centre of the CFB. Particle transportation occurs between the dilute region and dense region. This non-uniform particle distribution results from the existence of particle clusters and greatly influences the aerodynamic characteristics of CFBs (Grace and Bi 1997; Helland et al. 2007).

To understand the characteristics of gas-solids contacting in CFB, catalytic ozone decomposition reaction is often applied as a model reaction in a growing consensus in recent period (Kagawa et al. 1990; Jiang et al. 1990; Jiang et al. 1991; Bi et al. 1992; Ouyang, Lin, and Potter 1993; Ouyang, Li, and Potter 1995; Bolland and Nicolai 2001; Li 2010). During the fluidization in a CFB, catalytic decomposition of ozone into diatomic oxygen requires very low concentration of the ozone so that the gas density and temperature changes caused by the reaction in the CFB can be neglected. In addition, catalytic ozone decomposition reaction has an easily measurable first-order reaction rate at ambient temperature. Moreover, ozone detection technology is effective using fairly simple methods (Syamlal and O'Brien 2003). Thus, all these advantages make catalytic ozone decomposition the most widespread model reaction for the characterization of gas-solids contacting in fluidized bed reactors.

Although experiments are usually considered as more accurate, most experiments are expensive and difficult to measure the fluidization process with details. Thus, CFD is considered as a relatively more economical method to investigate the process in CFBs.

CFD is a subfield of fluid mechanics that uses numerical methods and algorithms to solve and analyze problems about fluid flows. Computers are the tool to execute the calculations required to simulate the interaction of fluid with surfaces defined by boundary conditions. With the high pace of technology development on high-performance supercomputers, some information like turbulence, which cannot be or are hard to be measured under laboratory conditions, can be easily obtained using CFD methods. Moreover, CFD tools can provide a more comprehensive data profile without disturbing the flow via internal probes (Ranade 2002). More important, they can require less time compared with experimental methods.

1.2 Literature review

To solve the solids phase in multiple phase flow, generally, there are two methods, the Eulerian-Lagrangian approach and Eulerian-Eulerian approach.

In the Eulerian-Lagrangian model, the solids phase is solved as a discrete phase by tracking a large number of particles based on Lagrangian force balance equations. However, there is a basic underlying assumption in the Eulerian-Lagrangian model that the dispersed second phase should be in a very low volume fraction. The particles are computed respectively at specified intervals during the fluid phase calculation (Tsuji, Kawaguchi, and Tanaka 1993; Tsuji, Tanaka, and Yonemura 1998; Tanaka et al. 1996;

Gera et al. 1998; Ouyang and Li 1999). This assumption implies that the model is only suitable for the simulations of some particle-laden flows, spray dryers, coal and liquid fuel combustion, not for the modeling of fluidized beds, or any case where the volume fraction of the second phase cannot be neglected.

With the other method, the Eulerian-Eulerian approach, both solids and fluid phases are solved by Navier–Stokes equations coupling with pressure and interphase exchange coefficient (Wen and Yu 1966; Syamlal and O'Brien 1986; Gidaspow, Bezburuah, and Ding 1992). Any number and type of second phase can be modeled. The drawbacks of the Eulerian-Eulerian method are the requirement of large computer memory and convergence difficulty due to a large amount of equations to be solved for each phase.

To describe the particle motion, the kinetic theory of granular flow was proposed by analogy between the random motion of particles caused by particle-particle collisions and the thermal motion of molecules to derive the theoretical expression of solids stress. Granular temperature was introduced to be proportional to the kinetic energy of the particle random motion taking the analogy to the temperature of the gas (Ding and Gidaspow 1990). This granular kinetic theory explains the mechanism of solids viscosity which is widely used in studies for gas-solids two-phase flows. The research on CFD modeling of gas-solids flows in fluidized beds has made great progresses in past decades. The Eulerian-Eulerian approach with the kinetic theory of granular flow is the most acceptable method to simulate gas-solids flows in CFB (Cruz, Steward, and Pugsley 2006; Almuttahar and Taghipour 2008; Wang et al. 2010; Peng, Zhu, and Zhang 2010).

A grid resolution study on gas-solids flow showed the grid size has critical influences on the numerical results considering the small particle size. It was suggested that the mesh size to solve gas-solids flows should be within the order of 10-50 particle diameters. Grid size close to 10 times of the particle diameter can be a critical value to ensure the numerical simulation is steady (Agrawal et al. 2001; Andrews IV, Loezos, and Sundaresan 2005). Actually the grid captures the particle clusters rather than individual particles. The particle cluster is considered as a mesoscale structure arisen as a result of an instable motion between gas and particle phases, the length scale of which is about 10 times the particle size. If the grid size is smaller than this length scale, the fluctuation will be revealed (Zhang and VanderHeyden 2001; Agrawal et al. 2001; Andrews IV, Loezos, and Sundaresan 2005). At the same time, a longer simulation flow time can provide more steady results (Ibsen and Hjertager 2001).

The effect of the inlet distributor of a CFB riser on the core-annulus structure of solid particles was studied in the previous work (Peng, Zhu, and Zhang 2010). Different distributions of nozzles on the distributor will result in different radial profiles for solids volume fraction. Using jets inlet approach as the inlet boundary condition predicts better solids distribution mimicking experimental results (Peng, Zhu, and Zhang 2010).

The wall in a CFB has a strong effect on the particle distribution as shown by experiments (Savage and Sayed 1984; Craig, Buckholz, and Domoto 1987; Qi, Zhang, and Zhu 2008). In term of the Jackson and Johnson wall boundary condition (Johnson and Jackson 1987), the specularity coefficient and particle-wall restitution coefficient were

introduced to define the wall conditions numerically. The former describes the roughness of the wall to determine the momentum transfer due to the collision between the particle and wall with the value between 0 for perfectly specular collision and 1 for perfectly diffuse collision. The latter is the coefficient determining the dissipation energy per particle-wall collision. The effect of these two coefficients on solid particle distributions has been studied and reported with the same conclusion that specularity coefficient strongly affects the core-annulus structure of solids near the wall where particle-wall restitution coefficient only plays a minor role (Benyahiaa, Syamlala, and O'Brien 2005; Almuttahar and Taghipour 2008; Wang et al. 2010; Li, Grace, and Bi 2010; Lan et al. 2012). Moreover, in CFB, low specularity coefficient can lead to good results comparing to experimental results (Benyahia, Syamlal, and O'Brien 2007; Almuttahar and Taghipour 2008; Wang et al. 2010). However the studies were all executed by comparing one of the two coefficients with different values when the other one was fixed. The interaction between the two coefficients has not been investigated. Then, for a CFB, the solid particle distribution strongly depends on the particle velocity, but the effect of wall boundary conditions on particle velocity was ignored. Moreover, as the coefficients defining the physical property of wall, there is no generality test under different operating conditions

Very few works have been reported in the literature on the coupling between detailed aerodynamic modeling and chemical reactions in CFB systems. Therdthianwong et al (2003) modeled 2D ozone decomposition reaction in a CFB riser, but the predicted solids distribution was not a typical core-annulus structure and the ozone concentration did

not match well with the particle distribution. Hansen et al (2004) and Dong et al (2008) reported the results about the simulation of ozone decomposition reaction in a gas-solids CFB riser with kinetic theory of granular flow with a good agreement with experiments, but the numerical solutions of ozone concentrations and solid volume fraction presented oscillated in a range between 5% and 50% of the average value, which indicated convergence problems, although they matched the experiments data well at certain flow time. Moreover, the reaction rate equation was not with respect to particle surface, which can not reflect the effect of the particle sizes in the reaction.

Based on the above literature review on CFD studies in aerodynamics and reactions for gas-solids two-phase flow in fluidized beds, the following points can be concluded, which will be investigated in this study:

(1) No CFD study has provided a comprehensive mapping of aerodynamic parameters and reactant concentrations in the axial and radial profiles in CFBs.

(2) No CFD study has been done on the sensitivity of wall boundary conditions on particle distributions under different operating conditions (superficial gas velocity and solid particle circulation rate).

1.3 Research objectives

Based on those discussed in the previous section, the objectives of this study are:

(1) To develop a complete numerical model coupling aerodynamic flow and chemical reactions using the granular kinetic theory for the fluid flow and chemical reactions

in gas-solids CFB risers.

(2) To study the effect of the wall boundary conditions on solids distributions in CFB risers.

(3) To compare aerodynamics and reactant concentration between numerical and experimental result to validate the proposed numerical model.

1.4 Thesis structure

This thesis is in the “Integrated-Article Format”. The structure is as follows:

(1) Chapter 1 gives a brief introduction and literature review on CFD modeling on gas-solids flows in CFB risers.

(2) Chapter 2 describes the configuration of the CFB riser used in this study and the CFD model for the simulation of the gas-solids two-phase flow and catalytic ozone decomposition in a CFB riser.

(3) Chapter 3 presents the effect of wall boundary conditions on the solid particle distribution in a CFB riser.

(4) Chapter 4 provides a comparison of the radial and axial profiles for the reactant concentration of catalytic ozone decomposition reaction between simulation and experiments.

(5) Chapter 5 gives conclusions of this research and recommendations for future work.

References

Agrawal, K., Leozos, P. N., Syamlal, M., & Sundarensan, S. (2001). The role of meso-scale structures in rapid gas-solid flows. *J. Fluid Mech. , 445*, p. 151-185.

Almuttahar, A., & Taghipour, F. (2008). Computational fluid dynamics of high density circulating fluidized bed riser: Study of modeling parameters. *Powder Technology , 185*, pp. 11-23.

Andrews IV, A. T., Loezos, P. N., & Sundaresan, S. (2005). Coarse-grid simulation of gas-particle flows in vertical risers. *Ind. Eng. Chem. Res. , 44*, pp. 6022-6037.

Benyahia, S., Syamlal, M., & O'Brien, T. J. (2007). Study of the ability of multiphase continuum models to predict core-annulus flow. *AIChE Journal , 53* (10), pp. 2549-2568.

Benyahiaa, S., Syamlala, M., & O'Brien, T. J. (2005). Evaluation of boundary conditions used to model dilute, turbulent gas/solids flows in a pipe. *Powder Technology , 156*, pp. 62 – 72.

Bi, H., Jiang, P., Jean, R. H., & Fan, L. S. (1992). Coarse-particle effects in a multisolid circulating fluidized bed for catalytic reactions. *Chemical Engineering Science , 47* (12), pp. 3113-3124.

Bolland, O., & Nicolai, R. (2001). Describing mass transfer in circulating fluidized beds by ozone decomposition. *Chemical Engineering Communications , 187* (1), pp. 1-21.

Craig, K., Buckholz, R. H., & Domoto, G. (1987). Effect of shear surface boundaries on stress for shearing flow of dry metal powders — an experimental-study. *Journal of Tribology-Transactions of the ASME , 109* (2), pp. 232–237.

Cruz, E., Steward, F. R., & Pugsley, T. (2006). New closure models for CFD modeling of high-density circulating fluidized beds. *Powder Technology , 169*, pp. 115–122.

Ding, J., & Gidaspow, D. (1990). A bubbling fluidization model using kinetic theory of granular flow. *AIChE Journal , 36* (4), pp. 523–538.

Dong, W. G., Wang, W., & Li, J. H. (2008). A multiscale mass transfer model for gas–solid riser flows: part II—sub-grid simulation of ozone decomposition. *Chemical Engineering Science , 63*, pp. 2811 – 2823.

Gera, D., Gautam, M., Tsuji, T., Kawaguchi, T., & Tanaka, T. (1998). Computer simulation of bubbles in large particle fluidized beds. *Powder Technol , 98* (1), pp. 38-47.

Gidaspow, D., Bezburuah, R., & Ding, J. (1992). Hydrodynamics of circulating fluidized beds, kinetic theory approach. In *Fluidization VII: Proceedings of the 7th Engineering Foundation Conference on Fluidization.* 75-82.

Grace, J. R. (1990). High-velocity fluidized bed reactors. *Chemical Engineering Science , 45* (8), pp. 1953–1966.

Grace, J. R., & Bi, H. (1997). Introduction to circulating fluidized beds. In J. R. Grace, A. Avidan, & T. Knowlton, *Circulating fluidized beds* (pp. 1-19). New York: Engineering Foundation.

Hansen, K. G., Solberg, T., & Hjertager, B. H. (2004). A three-dimensional simulation of gas/particle flowand ozone decomposition in the riser of a circulating fluidized bed. *Chemical Engineering Science , 59*, pp. 5217 – 5224.

Helland, E., Bournot, H., Occelli, R., & Tadrist, L. (2007). Drag reduction and cluster formation in a circulating fluidised bed. *Chemical Engineering Science , 62* (1-2), pp. 148-158.

Huang, W., Yan, A., & Zhu, J. (2007). Hydrodynamics and flow development in a 15.1 m circulating fluidized bed riser. *Chem. Eng. & Technol , 30* (4), pp. 460-466.

Huang, W., Zhu, J., & Parssinen, J. H. (2006). Comprehensive study on solids acceleration length in a long CFB riser. *29* (10), 1197-1204.

Ibsen, C. H., & Hjertager, B. H. (2001). Evaluation of a three-dimensional numerical model of a scaled. *Ind. Eng. Chem. , 40*, pp. 5081-5086.

Jiang, P., Bi, H., Jean, R. H., & Fan, L. S. (1991). Baffle effects on performance of catalytic circulating fluidized bed reactor. *AIChE Journal , 37* (9), 1392-1400.

Jiang, P., Inokuchi, K., Jean, R. H., Bi, H., & Fan, L. S. (1990). Ozone decomposition in a catalytic circulating fluidized bed reactor. In P. Basu, M. Horio, & M. Hasatani, *Circulating Fluidized Bed Technology III* (pp. 557-562). Oxford: Pergamon Press.

Johnson, P. C., & Jackson, R. (1987). Frictional-collisional constitutive relations for granular materials, with application to plane shearing. *J. Fluid Mech. , 176*, pp. 67-93.

Kagawa, H., Mineo, H., Yamazaki, R., & Yoshida, K. (1990). A gas-solid contacting model for fast fluidized bed. In P. Basu, M. Horio, & M. Hasatani, *Circulating Fluidized Bed Technology III* (pp. 551-556). Oxford: Pergamon Press.

Lan, X. Y., Xu, C. M., Gao, J. S., & Al-Dahhan, M. (2012). Influence of solid-phase wall boundary condition on CFD simulation of spouted beds. *Chemical Engineering Science , 69*, pp. 419-430.

Li, D. B. (2010). *Investigation of circulating fluizied bed riser and downer reactor performance for catalytic ozone decompostion.* Phd Thesis, Univ. of Western Onatario.

Li, T. W., Grace, J., & Bi, X. T. (2010). Study of wall boundary condition in numerical simulations of bubbling fluidized beds. *Powder Technology , 203*, pp. 447-457.

Miller, A., & Gidaspow, D. (1992). Dense, vertical gas–solids flow in a pipe. *AIChE J. , 38*, pp. 1801-1813.

Ouyang, J., & Li, J. (1999). Particle motion resolved discrete model for simulating gas solid fluidization. *Chem. Eng. Sci. , 54*, pp. 2077-2083.

Ouyang, S., Li, X. G., & Potter, O. E. (1995). Circulating fluidized bed as a catalytic reactor: experimental study. *AIChE Journal , 41* (6), pp. 1534–1542.

Ouyang, S., Lin, J., & Potter, O. E. (1993). Ozone decomposition in a 0.254 m diameter circulating fluidized bed reactor. *Powder Technology , 74* (1), pp. 73-78.

Peng, B. T., Zhu, J., & Zhang, C. (2010). Numerical study on the effect of the air jets at the inlet distributor in the gas-solids circulating fluidized-bed risers. *Ind. Eng. Chem. Res. , 49*, pp. 5310–5322.

Qi, X. B., Zhang, H., & Zhu, J. (2008). Friction between gas–solid flow and circulating fluidized bed downer wall. *Chemical Engineering Journal , 142*, pp. 318–326.

Qi, X., Huang, W., Pan, Y., Zhu, J., & Shi, Y. (2003). Investigation on solids concentration and core-annulus flow structure in circulating fluidized bed risers. *J. Sichuan Univ. , 35* (1), pp. 43-47.

Ranade, V. (2002). Computational flow modeling for chemical reactor engineering. New York: Academic Press.

Reh, L. (1999). Challenges of circulating fluid-bed reactors in energy and raw materials industries. *Chemical Engineering Science , 54* (22), pp. 5359–5368.

Savage, S. B., & Sayed, M. (1984). Stresses developed by dry cohesionless granular-materials sheared in an annular shear cell. *Journal of Fluid Mechanics , 142*, pp. 391–430.

Syamlal, M., & O'Brien, T. (1986). Computer simulation of bubbles in a fluidized bed. *AIChE Symposium Series , 85*, pp. 22-31.

Syamlal, M., & O'Brien, T. (2003). Fluid dynamic simulation of O3 decomposition in a bubbling fluidized bed. *AIChE Journal , 49* (11), pp. 2793–2801.

Tanaka, T., Yonemura, S., Kiribayashi, K., & Tsuji, Y. (1996). Cluster formation and particle induced instability in gas solid flows predicted by the DSMC method. *JSME international journal series B-fluids and thermal engineering , 39* (2), pp. 239-245.

Therdthianwong, A., Pantaraks, P., & Therdthianwong, S. (2003). Modeling and simulation of circulating fluidized bed reactor with catalytic ozone decomposition reaction. *Powder Technology , 133*, pp. 1– 14.

Tsuji, Y., Kawaguchi, T., & Tanaka, T. (1993). Discrete particles simulation of 2. *Powder Technol , 77* (1), pp. 79-87.

Tsuji, Y., Tanaka, T., & Yonemura, S. (1998). Cluster patens in circulating fluidized beds predicted by numerical simulation (discrete particles model versus two fluid model). *Powder Technol , 3*, pp. 254-264.

Wang, X. F., Jin, B. S., Zhong, W. Q., & Xiao, R. (2010). Modeling on the hydrodynamics of a high-flux circulating fluidized bed with geldart group a particles by kinetic theory of granular flow. *Energy Fuels , 24*, pp. 1242–1259.

Wen, C. Y., & Yu, Y. H. (1966). Mechanics of Fluidization. *Chem. Eng. Prog. Symp. Series , 62*, pp. 100–111.

Yan, A., & Zhu, J. (2004). Scale-up effect of riser reactors (1) axial and radial solids concentration distribution and flow development. *Ind & Eng Chem Res , 43* (19), pp. 5810-5819.

Yerushalmi, J., Turner, D. H., & Squires, A. M. (1976). The fast fluidized bed. *Industrial & Engineering Chemistry Process Design and Development , 15* (1), pp. 47–53.

Zhang, D. Z., & VanderHeyden, W. B. (2001). High-resolution three-dimensional numerical simulation of a circulating fluidized bed. *Powder Technology , 116*, pp. 133–141.

Zhu, J. X., & Cheng, Y. (2005). Fluidized-Bed Reactors and Applications. In C. Crowe (Ed.), *Multiphase Flow Handbook* (pp. 5.55-5.93). New York: CRC Press.

Chapter 2.

2 Configuration of the CFB riser and numerical models

In this chapter configuration of the CFB riser used in this study is introduced first. Then the numerical models for the gas-solids two-phase simulations are presented.

2.1 Configuration of the CFB riser

The CFB riser used in this study is from the previous work by Li (2010), where the catalytic ozone decomposition experiment was carried out. The CFB system is illustrated in Figure 2.1. The riser is 10m in height with 76.2 mm inner diameter. The mixed gas is supplied from the nozzles on the distributor located at the bottom of the riser, which are shown on Figure 2.2. It should be noticed that the distributor is not completely axisymmetric. Solid particles from the storage tank are fluidized by the gas from the perforated distributor plate towards the top of the riser. Due to the height of riser, the two-phase flow can achieve fully developed flow.

The air supplied from the bottom of the riser contained about 20 ppm ozone. The decomposition of ozone to oxygen is a thermodynamically favoured process (Wojtowicz 2005). However, the ozone decomposition reaction under room temperature is slow in the lack of catalysts and ultraviolet light. Therefore, catalysts are requisite to decompose it under ambient temperatures (Dhandapani and Oyama 1997; Lin and Nakajima 2002). The solid particles are fresh FCC catalyst particles.

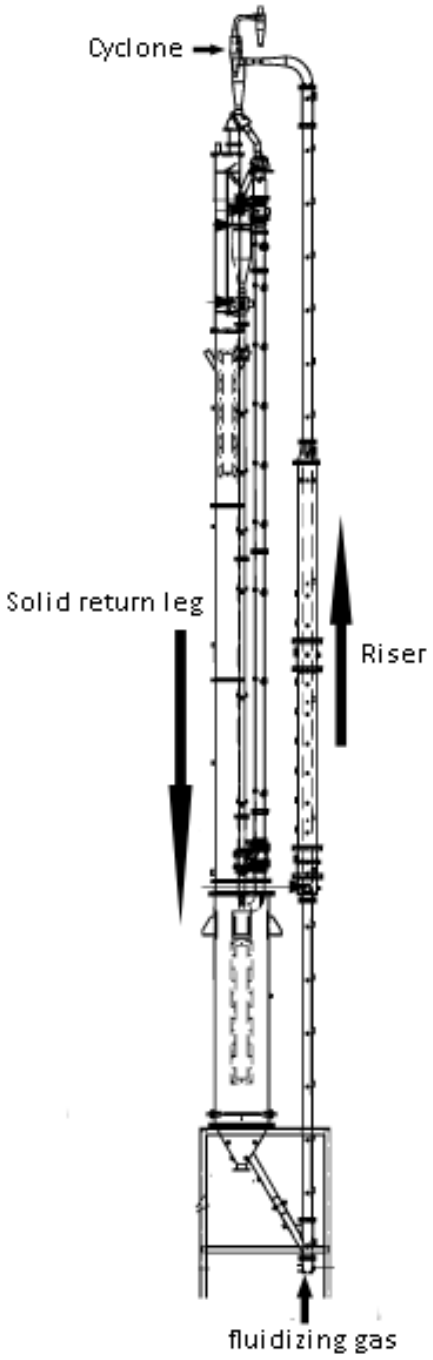

Figure 2.1 Configuration of the CFB system (Li 2010)

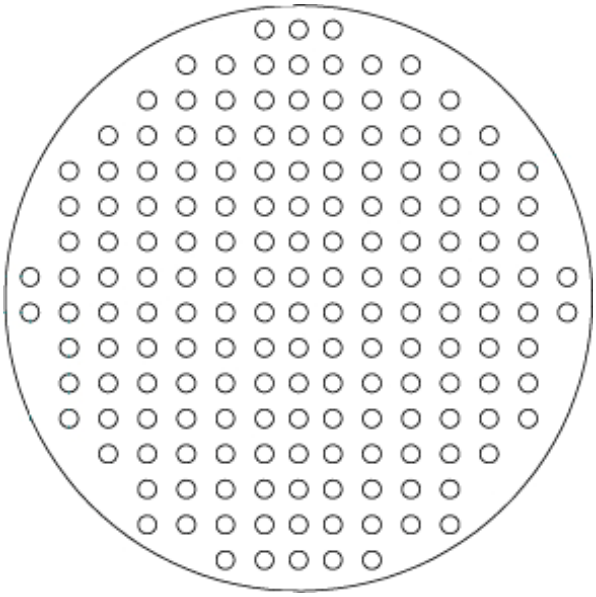

Figure 2.2 Inlet distributor of the riser (Li 2010)

The experiments were conducted by Li (2010) under the operating conditions of superficial velocities of 3 m/s and 5 m/s with solids circulation rates being 50 kg/($m^2 \cdot s$) and 100 kg/($m^2 \cdot s$), respectively. The available experimental data reported by Li (2010) are at 0.11m, 1.02m, 2.39m, 4.78m, 7.32m and 9.61m above the gas distributor of the riser. The radial positions are r/R= 0, 0.316, 0.548 0.707, 0.837 and 0.949, respectively.

2.2 Numerical model

2.2.1 Governing equations

The Eulerian-Eulerian method is employed in this study due to high solids volume fraction in the CFB riser. The solids phase is treated as a continuum phase solved by mass and momentum transported equations similar to those for the fluid phase. The momentum exchange is coupled by pressure and interphase exchange coefficient. The solids pressure is calculated in the compressive regime. Due to collisions of between

particles, granular temperature is introduced to be proportional to the kinetic energy of the particles random motion taking the analogy to the temperature of the gas (Ding and Gidaspow 1990). The governing equations using a k-ε turbulence model for each phase are solved using the finite volume method. The equations are listed as follows:

Conservation equation of mass for the gas phase

$$\frac{\partial}{\partial t}\left(\alpha_g \rho_g\right) + \nabla \cdot \left(\alpha_g \rho_g \vec{v}_g\right) = 0 \quad (1)$$

Conservation equation of mass for the solids phase

$$\frac{\partial}{\partial t}\left(\alpha_s \rho_s\right) + \nabla \cdot \left(\alpha_s \rho_s \vec{v}_s\right) = 0 \quad (2)$$

α is volume fraction and $\alpha_g + \alpha_s = 1$

Conservation equation of momentum for the gas phase

$$\frac{\partial}{\partial t}\left(\alpha_g \rho_g \vec{v}_g\right) + \nabla \cdot \left(\alpha_g \rho_g \vec{v}_g \vec{v}_g\right) = -\alpha_g \nabla p + \nabla \cdot \left(\overline{\overline{\tau_{g,m}}} + \overline{\overline{\tau_{g,t}}}\right) + \alpha_g \rho_g \vec{g} + K_{sg}\left(\vec{v}_s - \vec{v}_g\right) \quad (3)$$

where

$$\overline{\overline{\tau_{g,m}}} = \alpha_g \mu_{g,m}\left(\nabla \vec{v}_g + \nabla \vec{v}_g{}^T\right) - \frac{2}{3}\alpha_g \mu_{g,m} \nabla \cdot \vec{v}_g \, \bar{\bar{I}}$$

$$\overline{\overline{\tau_{g,t}}} = -\frac{2}{3}\alpha_g \rho_g k_g \bar{\bar{I}} + \alpha_g \mu_{g,t}\left(\nabla \vec{v}_g + \nabla \vec{v}_g{}^T\right) - \frac{2}{3}\alpha_g \mu_{g,t} \nabla \cdot \vec{v}_g \, \bar{\bar{I}}$$

Conservation equation of momentum for the solids phase

$$\frac{\partial}{\partial t}\left(\alpha_s \rho_s \vec{v}_s\right) + \nabla \cdot \left(\alpha_s \rho_s \vec{v}_s \vec{v}_s\right) = -\alpha_s \nabla p - \nabla p_s + \nabla \cdot \left(\overline{\overline{\tau_{s,m}}} + \overline{\overline{\tau_{s,t}}}\right) + \alpha_s \rho_s \vec{s} + K_{gs}\left(\vec{v}_g - \vec{v}_s\right) \quad (4)$$

where

$$\overline{\overline{\tau_{s,m}}} = \alpha_s \mu_{s,m}\left(\nabla \vec{v}_s + \nabla \vec{v}_s^{\,T}\right) - \frac{2}{3}\alpha_s \mu_{s,m} \nabla \cdot \vec{v}_s \,\overline{\overline{I}} + \lambda_s \nabla \cdot \vec{v}_s \,\overline{\overline{I}}$$

$$\overline{\overline{\tau_{s,t}}} = -\frac{2}{3}\alpha_s \rho_s k_s \overline{\overline{I}} + \alpha_s \mu_{s,t}\left(\nabla \vec{v}_s + \nabla \vec{v}_s^{\,T}\right) - \frac{2}{3}\alpha_s \mu_{s,t} \nabla \cdot \vec{v}_s \,\overline{\overline{I}}$$

K is the interphase exchange coefficient and $K_{gs}=K_{sg}$. In the Syamlal-O'Brien model (Syamlal and O'Brien 1986), this value is based on measurements of terminal velocity $v_{s,\gamma}$:

$$K_{sg} = \frac{3\alpha_s \alpha_g \rho_g}{4 v_{s,\gamma}^2 d_s}\left(0.63 + \frac{4.8}{\sqrt{Re_s / v_{s,\gamma}}}\right)^2 \left(\frac{Re_s}{v_{s,\gamma}}\right)\left|\vec{v}_s - \vec{v}_g\right| \quad (5)$$

$$v_{s,\gamma} = 0.5\left(A - 0.06 Re_s + \sqrt{(0.06 Re_s)^2 + 0.12 Re_s (2B - A) + A^2}\right) \quad (6)$$

where $A=\alpha_g^{4.14}$, $B=0.8\alpha_g^{1.28}$ for $\alpha_g \leq 0.85$ and $B=a_g^{2.65}$ for $\alpha>0.85$ and $Re_s = \frac{\rho_g d_s \left|\vec{v}_s - \vec{v}_g\right|}{\mu_{g,m}}$

The solids pressure and viscosity are related to the granular temperature θ_s based on the kinetic theory of the granular flow. In the Syamlal-O'Brien model (Syamlal and O'Brien 1986), it is expressed by

$$p_s = 2\rho_s(1+e_{ss})\alpha_s^2 g_{s,0}\Theta_s \tag{7}$$

where $g_{s,0}$ is radial distribution function $g_{s,0} = \left[1-\left(\frac{\alpha_s}{\alpha_{s,max}}\right)^{\frac{1}{3}}\right]^{-1}$.

Solids shear viscosity

$$\mu_s = \mu_{s,m} = \mu_{s,col} + \mu_{s,kin} \tag{8}$$

Collisional viscosity

$$\mu_{s,col} = \frac{4}{5}{\alpha_s}^2\rho_s d_s g_{s,0}(1+e_{ss})\left(\frac{\Theta_s}{\pi}\right)^{1/2} \tag{9}$$

Kinetic viscosity

$$\mu_{s,kin} = \frac{\alpha_s\rho_s d_s\sqrt{\Theta_s\pi}}{6(3-e_{ss})}\left[1+\frac{2}{5}g_{s,0}\alpha_s(1+e_{ss})(3e_{ss}-1)\right] \tag{10}$$

Bulk viscosity

$$\lambda_s = \frac{4}{3}\alpha_s\rho_s d_s g_{s,0}(1+e_{ss})\left(\frac{\Theta_s}{\pi}\right)^{1/2} \tag{11}$$

e_{ss} is the particle-particle restitution coefficient taken as empirical value 0.95 (Peng, Zhu, and Zhang 2010).

Granular temperature Θ_s is obtained by solving its transport equation:

$$\frac{3}{2}\left[\frac{\partial}{\partial t}\left(\rho_s \alpha_s \Theta_s\right) + \nabla \cdot \left(\rho_s \alpha_s \vec{v}_s \Theta_s\right)\right] = \left[-p_s \bar{\bar{I}} + \left(\bar{\bar{\tau}}_s^m + \bar{\bar{\tau}}_s^t\right)\right] : \nabla \vec{v}_s + \nabla \cdot \left(k_{\Theta_s} \nabla \Theta_s\right) - \gamma_{\Theta_s} + \Phi_{gs} \quad (12)$$

The diffusion coefficient of energy:

$$k_{\Theta_s} = \frac{15 \alpha_s \rho_s d_s \sqrt{\Theta_s \pi}}{4(41 - 33\eta)}\left[1 + \frac{12}{5}\eta^2(4\eta - 3)\alpha_s g_{s,0} + \frac{16}{15\pi}(41 - 33\eta)\eta \alpha_s g_{s,0}\right] \quad (13)$$

where $\eta = 1/2(1+e_{ss})$.

The collisional dissipation of energy:

$$\gamma_{\Theta_s} = \frac{12(1 - e_s^2) g_{s,0}}{d_s \sqrt{\pi}} \rho_s {\alpha_s}^2 {\Theta_s}^{3/2} \quad (14)$$

and the energy exchange between two phases is defined as $\Phi_{gs} = -3K_{gs}\Theta_s$

k*-ε *turbulence model for the gas phase

$$\frac{\partial}{\partial t}\left(\alpha_g \rho_g k_g\right) + \nabla \cdot \left(\alpha_g \rho_g \vec{v}_g k_g\right) = \nabla \cdot \left(\alpha_g \left(\mu_{g,m} + \frac{\mu_{g,t}}{\sigma_k}\right) \nabla k_g\right) + \left(\alpha_g G_{g,k} - \alpha_g \rho_g \varepsilon_g\right) + K_{sg}\left(C_{sg} k_s - C_{gs} k_g\right) - K_{sg}\left(\vec{v}_s - \vec{v}_g\right)\frac{\mu_{s,t}}{\alpha_s \sigma_s}\nabla \alpha_s + K_{sg}\left(\vec{v}_s - \vec{v}_g\right)\frac{\mu_{g,t}}{\alpha_g \sigma_g}\nabla \alpha_g \quad (15)$$

$$\frac{\partial}{\partial t}\left(\alpha_g \rho_g \varepsilon_g\right) + \nabla \cdot \left(\alpha_g \rho_g \vec{v}_g \varepsilon_g\right) = \nabla \cdot \left(\alpha_g \frac{\mu_{g,t}}{\sigma_\alpha} \nabla \varepsilon_g\right) + \frac{\varepsilon_g}{k_g}\Bigg\{ C_{1\varepsilon} \alpha_g G_{g,k} - C_{2\varepsilon} \alpha_g \rho_g \varepsilon_g + C_{3\varepsilon}\Bigg[K_{sg}\left(C_{sg}\, k_s - C_{gs}\, k_g\right) - K_{sg}\left(\vec{v}_s - \vec{v}_g\right) \frac{\mu_{s,t}}{\alpha_s \sigma_s} \nabla \alpha_s + K_{sg}\left(\vec{v}_s - \vec{v}_g\right) \frac{\mu_{g,t}}{\alpha_g \sigma_g} \nabla \alpha_g \Bigg]\Bigg\} \quad (16)$$

where $\mu_{g,t} = \rho_g C_\mu \frac{k_g^2}{\varepsilon_g}$ and $C_\mu = 0.09$.

k*-ε *turbulence model for the solids phase:

$$\frac{\partial}{\partial t}\left(\alpha_s \rho_s k_s\right) + \nabla \cdot \left(\alpha_s \rho_s \vec{v}_s\, k_s\right) = \nabla \cdot \left(\alpha_s \left(\mu_{s,m} + \frac{\mu_{s,t}}{\sigma_k}\right) \nabla k_s\right) + \left(\alpha_s G_{s,k} - \alpha_s \rho_s \varepsilon_s\right) + K_{gs}\left(C_{gs}\, k_g - C_{sg}\, k_s\right) - K_{gs}\left(\vec{v}_g - \vec{v}_s\right) \frac{\mu_{g,t}}{\alpha_g \sigma_g} \nabla \alpha_g + K_{gs}\left(\vec{v}_g - \vec{v}_s\right) \frac{\mu_{s,t}}{\alpha_s \sigma_s} \nabla \alpha_s \quad (17)$$

$$\begin{aligned}\frac{\partial}{\partial t}(\alpha_s\rho_s\varepsilon_s) + \nabla\cdot(\alpha_s\rho_s\,\vec{v}_s\,\varepsilon_s) \\ = \nabla\cdot\left(\alpha_s\frac{\mu_{s,t}}{\sigma_\alpha}\nabla\varepsilon_s\right) \\ + \frac{\varepsilon_s}{k_s}\Big\{C_{1\varepsilon}\alpha_s G_{s,k} - C_{2\varepsilon}\alpha_s\rho_s\varepsilon_s \\ + C_{3\varepsilon}\Big[K_{gs}(C_{gs}\,k_g - C_{sg}\,k_s) - K_{gs}(\vec{v}_g - \vec{v}_s)\frac{\mu_{g,t}}{\alpha_g\sigma_g}\nabla\alpha_g \\ + K_{gs}(\vec{v}_g - \vec{v}_s)\frac{\mu_{s,t}}{\alpha_s\sigma_s}\nabla\alpha_s\Big]\Big\}\end{aligned} \tag{18}$$

where $\mu_{s,t} = \rho_s C_\mu \frac{k_s^2}{\varepsilon_s}$ and $C_\mu = 0.09$.

Catalytic ozone decomposition

The catalytic ozone decomposition reaction is a simple irreversible first-order reaction expressed as $O_3 \xrightarrow{FCC} 1.5O_2$. The species transport equations are used to solve the mass fraction of each species in the mixture of the gases.

Ozone

$$\frac{\partial}{\partial t}\left(\alpha_g\rho_{O_3}Y_{O_3}\right) + \nabla\cdot\left(\alpha_g\rho_{O_3}\,\vec{v}_g\,Y_{O_3}\right) = -\nabla\cdot\alpha_g\bar{J}_{O_3} + R_{O_3} \tag{19}$$

where $\bar{J}_{O_3} = -(\rho_{O_3}D_{O_3} + \frac{\mu_{g,t}}{Sc_t})\nabla Y_{O_3}$, D is the mass diffusion coefficient and Sc_t is the turbulent Schmidt number.

Oxygen

$$\frac{\partial}{\partial t}\left(\alpha_g \rho_{O_2} Y_{O_2}\right) + \nabla \cdot \left(\alpha_g \rho_{O_2} \vec{v}_g Y_{O_2}\right) = -\nabla \cdot \alpha_g \bar{J}_{O_2} + R_{O_2} \quad (20)$$

where $\bar{J}_{O_2} = -(\rho_{O_2} D_{O_2} + \frac{\mu_{g,t}}{Sc_t})\nabla Y_{O_2}$.

R is the first-order reaction rate based on the catalyst particle volume. For ozone, it can be written as:

$$R_{O_3} = -\frac{\partial C_{O_3}}{\partial t} = W A_p k_r C_{O_3} \quad (21)$$

k_r is the reaction rate constant , which is determined by experimental data. It can also be expressed by Arrhenius equation $k_r = ze^{-E_a/rT}$. z, E_a, r and T are the pre-exponential factor, activation energy, universal gas constant and temperature respectively. According to the experiments, k_r =4x10^{-5}m/s (Li 2010). A_p is the particle surface area per unit volume. Assuming the shape of particles is sphere, so

$$A_p = \frac{\alpha_s}{\frac{1}{6}\pi d_s^3} \cdot \pi d_s^2 = \frac{6\alpha_s}{d_s} \quad (22)$$

and W is an empirical coefficient valued 0 to 1 to correct numerical reaction rate.

2.2.2 Computational domain and boundary conditions

Two-dimensional simulations of the CFB riser shown in Figure 2.1 are carried out in this study. The computational domain is of 10m × 0.0381m according to the dimensions of

the CFB riser. The schematic diagram of the computational domain and boundary conditions are shown in Figure 2.3. The boundary conditions at the inlet, outlet and wall are set up according to actual conditions in the riser.

Inlet: the profiles of the velocities of gas and solids, and volume fraction of solids are specified according to the geometry of the inlet distributor of the riser as well as the flow rates of both gas and solids phases. There are 6.5 jets along on the radius in the distributor as illustrated in Figure 2.4.

Outlet: the relative pressure at the outlet of the riser is specified as zero.

Wall: for the gas phase, no slip velocity on the wall is used. For the solids phase, the particles can slip on the wall based on the Jackson and Johnson theory (Johnson and Jackson 1987). The shear stress and collision energy are:

$$\tau_s = -\frac{\sqrt{3}\pi\rho_s g_{s,0}\alpha_s\phi\sqrt{\Theta_s}}{6\alpha_{s,max}} \tag{23}$$

$$q_s = \frac{\pi}{6}\sqrt{3}\phi\frac{\alpha_s}{\alpha_{s,max}}\rho_s g_{s,0}\sqrt{\theta_s}\upsilon_{s,w}^2 - \frac{\pi}{4}\sqrt{3}\frac{\alpha_s}{\alpha_{s,max}}\left(1-e_{s,w}^2\right)\rho_s g_{s,0}\theta_s^{\frac{3}{2}} \tag{24}$$

In Eqs. (23) and (24), ϕ is the specularity coefficient and $e_{s.w}$ is the particle-wall restitution coefficient. The second term in Eq. (24) represents the energy loss by collision between the particle and wall. The specularity coefficient describes the roughness of the wall to determine the momentum transfer due to the collision between the particle and wall with the value between 0 for perfectly specular collision

and 1 for perfectly diffuse collision. The particle-wall restitution coefficient is the parameter determining the dissipation energy per particle-wall collision. Both of the two parameters are empirical and to be determined from experimental results (Benyahiaa, Syamlala, and O'Brien 2005; Benyahia, Syamlal, and O'Brien 2007; Almuttahar and Taghipour 2008; Wang et al. 2010; Lan et al. 2012; Li, Grace, and Bi 2010).

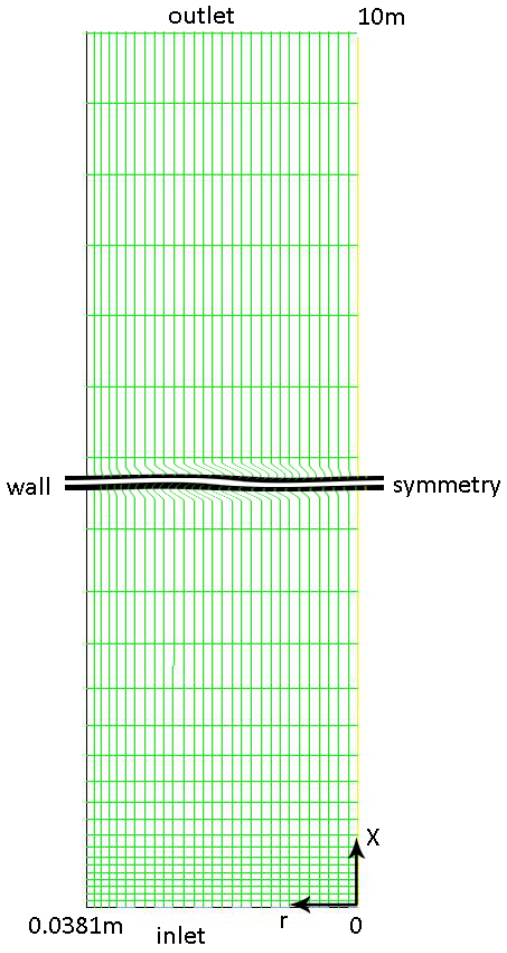

Figure 2.3 Computational domain, mesh and boundary conditions

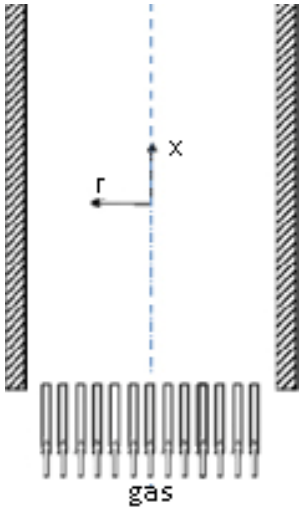

Figure 2.4 Schematic diagram of inlet boundary condition for the gas phase

2.2.3 Near wall treatment for wall bounded turbulent flow

The standard wall functions for wall bounded turbulent flows are based on the work of Launder and Spalding (Launder and Spalding 1974) and have been used widely for turbulent flow simulations. However, in the current study, if the standard wall functions are applied, the size of first grid from the wall has to be 1/3 of the radius of the riser to have the wall functions used in an acceptable region due to the low Reynolds number near the wall, which is not suitable to investigate the flow distributions in the near wall region in the riser.

Thus, the enhanced wall treatment is used in this study. In this method, the region where the standard wall functions used is divided into two regions – the viscosity layer and buffer layer. The first grid is located in the region where the viscosity dominates the flow and there are at least 10 grids in the buffer layer to capture the flow. So the enhanced wall treatment solves the viscosity affected layer, which standard wall

functions do not solve. However, the computational cost of using the enhanced wall treatment method is much higher than that of the standard wall functions

The demarcation of the wall region and full turbulence region is determined by a wall-distance based turbulent Reynolds number, $\mathrm{Re_y}$, defined as

$$\mathrm{Re_y} = \frac{\rho y\sqrt{k}}{\mu} \tag{24}$$

y is the distance from the nearest wall. When $\mathrm{Re_y} > 200$, the k-ε turbulence model is employed. In the viscosity affected region $(\mathrm{Re_y} < 200)$, the one-equation model of Wolfshtein (Wolfshtein 1969) is applied. In the one-equation model, the momentum equations and the k equation are the same as described above. However, the turbulent viscosity $\mu_{t,v}$ is calculated by:

$$\mu_{t,v} = \rho C_\mu l_\mu \sqrt{k} \tag{25}$$

where the length scale l_μ was derived by Chen and Patel (Chen and Patel 1988):

$$l_\mu = y C_l^* \left(1 - e^{-\mathrm{Re_y}/A_\mu}\right) \tag{26}$$

where $C_l^* = 0.4187 {C_\mu}^{-3/4}$, $A_\mu = 70$.

To prevent the solution convergence from being impeded when the turbulent viscosity from the main flow cannot match the turbulent viscosity of Wolfstern's equation, a blending function is proposed (Jongen 1992):

$$\mu_{t,enh} = \lambda_\varepsilon \mu_t + (1 - \lambda_\alpha)\mu_{t,v} \tag{27}$$

A blending function λ_ε is:

$$\lambda_\varepsilon = \frac{1}{2}\left\{1 + \tanh\left[\frac{\left|\mathrm{Re}_y - 200\right|\mathrm{artanh}(0.98)}{25}\right]\right\} \tag{28}$$

And ε in the viscosity affected region is determined by:

$$\varepsilon = \frac{k^{3/2}}{l_\varepsilon} \tag{29}$$

where $l_\varepsilon = yC_l^*\left(1 - e^{-\mathrm{Re}_y/A_\varepsilon}\right)$ and $A_\varepsilon = 2C_l^*$.

2.2.4 Mesh and Solver

The computational mesh is generated by ANSYS ICEM 13.0 with 12,093 rectangle cells. The double-precision segregated, implicit formulations and unsteady solver are selected in the simulation. The phase-coupled SIMPLE algorithm is applied for the pressure-based solver. The discretization scheme for all convection terms is the second-order upwind scheme except for the volume fraction equation where the QUICK scheme is used. A convergence criterion of 10^{-4} for each scaled residual component is specified except for the species fraction, where 10^{-5} is used. The commercial CFD software ANSYS FLUENT 13.0 is used to carry out the simulations with parallel 2.4Ghz CPU nodes. The operating conditions and parameters for the simulations are presented in Table 2.1.

Table 2.1 Operating conditions and parameters for simulations

Gas density ($\mathrm{kg/m^3}$)	1.225
Gas viscosity ($\mathrm{kg/(m \cdot s)}$)	1.7894×10^{-5}
Particle density ($\mathrm{kg/m^3}$)	1730
Particle diameter ($\mu\mathrm{m}$)	60, 120, 240
Superficial gas velocity ($\mathrm{m/s}$)	3, 5, 8.3
Particle circulation rate ($\mathrm{kg/(m^2 \cdot s)}$)	50, 100, 200
Particle-particle restitution coefficient	0.95
Particle-wall restitution coefficient	0.95, 0.9, 0.85
Specularity coefficient	0, 0.0001, 0.0002

Nomenclature

A_p = particle surface area per unit volume, m
C_{O3} = ozone concentration, ppm
C_μ = turbulence constant, dimensionless
$C_{1\varepsilon}$ = turbulence constant, dimensionless
$C_{2\varepsilon}$ = turbulence constant, dimensionless
$C_{3\varepsilon}$ = turbulence constant, dimensionless
D = mess diffusion coefficient, dimensionless
d = diameter, m
e= restitution coefficient, dimensionless
G_s = solids circulation rate, $kg/m^2 \cdot s^{-1}$
g = gravity, m/s^2
$g_{s,0}$ = radial distribution function, dimensionless
I = unit matrix, dimensionless
K = interphase exchange coefficient, $kg/m^3 \cdot s^{-1}$
k = turbulence kinetic energy, m^2/s^2
k_r = reaction rate constant, s^{-1}
$k_{\theta s}$= diffusion coefficient of energy, $kg/m \cdot s^{-1}$
p = pressure, Pa
q = collision energy, kg/s^{-3}
R= radius of the riser, m
r = radial coordinate, m
Re = Reynolds number, dimensionless
Sc_t = turbulent Schmidt number, dimensionless
t= time, s
v = velocity, m/s
x = axial coordinate, m
Y = species concentration, dimensionless

Greek symbols

α = volume fraction, dimensionless
γ = collision dissipation of energy, $kg/m \cdot s^{-3}$
ε = turbulence dissipation rate, m^2/s^3
θ = granular temperature, m^2/s^2
λ = bulk viscosity, $kg/m \cdot s^{-1}$
μ = viscosity, $kg/m \cdot s^{-1}$
ρ = density, kg/m^3
τ = stress tensor, Pa
Φ = energy exchange coefficient, $kg/m \cdot s^{-3}$
ϕ = specularity coefficient, dimensionless

Subscripts

g = gas phase
s = solids phase
m= molecular
t = turbulence
w= wall

References

Almuttahar, A., & Taghipour, F. (2008). Computational fluid dynamics of high density circulating fluidized bed riser: Study of modeling parameters. *Powder Technology , 185*, pp. 11-23.

Benyahia, S., Syamlal, M., & O'Brien, T. J. (2007). Study of the ability of multiphase continuum models to predict core-annulus flow. *AIChE Journal , 53* (10), pp. 2549-2568.

Benyahiaa, S., Syamlala, M., & O'Brien, T. J. (2005). Evaluation of boundary conditions used to model dilute, turbulent gas/solids flows in a pipe. *Powder Technology , 156*, pp. 62 – 72.

Chen, H. C., & Patel, V. C. (1988). Near-wall turbulence models for complex flows including separation. *AIAA Journal , 6*, pp. 641–648.

Dhandapani, B., & Oyama, S. (1997). Gas phase ozone decomposition catalysts. *Applied Catalysis B: Environmental , 11* (2), pp. 129–166.

Ding, J., & Gidaspow, D. (1990). A bubbling fluidization model using kinetic theory of granular flow. *AIChE Journal , 36* (4), pp. 523–538.

Johnson, P. C., & Jackson, R. (1987). Frictional-collisional constitutive relations for granular materials, with application to plane shearing. *J. Fluid Mech. , 176*, pp. 67-93.

Jongen, T. (1992). *Simulation and modeling of turbulent incompressible flows.* PhD thesis, EPF Lausanne, Lausanne.

Lan, X. Y., Xu, C. M., Gao, J. S., & Al-Dahhan, M. (2012). Influence of solid-phase wall boundary condition on CFD simulation of spouted beds. *Chemical Engineering Science , 69*, pp. 419-430.

Launder, B., & Spalding, D. (1974). The numerical computation of turbulent flows. *Computer Methods in Applied Mechanics and Engineering , 3*, pp. 269–289.

Li, D. B. (2010). *Investigation of circulating fluizied bed riser and downer reactor performance for catalytic ozone decompostion.* Phd Thesis, Univ. of Western Onatario.

Li, T. W., Grace, J., & Bi, X. T. (2010). Study of wall boundary condition in numerical simulations of bubbling fluidized beds. *Powder Technology , 203*, pp. 447-457.

Lin, J., & Nakajima, T. (2002). An AM1 study of decomposition of ozone on a Cu(110) surface. *Ozone: Science & Engineering: The Journal of the International Ozone Association , 24* (1), pp. 39–47.

Syamlal, M., & O'Brien, T. (1986). Computer simulation of bubbles in a fluidized bed. *AIChE Symposium Series , 85*, pp. 22-31.

Wang, X. F., Jin, B. S., Zhong, W. Q., & Xiao, R. (2010). Modeling on the hydrodynamics of a high-flux circulating fluidized bed with geldart group a particles by kinetic theory of granular flow. *Energy Fuels , 24*, pp. 1242–1259.

Wojtowicz, J. A. (2005). Ozone. In J. Wiley, & Sons, *Kirk-Othmer encyclopedia of chemical technology.*

Wolfshtein, M. (1969). The velocity and temperature distribution of one-dimensional flow with turbulence augmentation and pressure gradient. *Int. J. Heat Mass Transfer. , 12*, pp. 301–318.

Chapter 3.

3 Evaluation of the effect of wall boundary conditions on numerical simulations of circulating fluidized beds

3.1 Introduction

A gas-solids circulating fluidized bed (CFB) is a reactor device based on the fluidization phenomenon between gas and particles operated under high gas velocity in the circulating flow regime, which can be applied to implement a variety of multiphase chemical reactions. The advantages of CFB, i.e. higher gas-solids contact efficiency, reduced axial dispersion for both gas and solids phases and higher gas-solids throughput have been reported by researchers in past two decades (Grace 1990; Reh 1999; Zhu and Cheng 2005).

During the fluidization process, there is a non-uniform radial distribution of the solid particles in CFB risers, which is known as core-annulus structure (Qi et al. 2003; Yan and Zhu 2004; Huang, Zhu, and Parssinen 2006; Huang, Yan, and Zhu 2007; Miller and Gidaspow 1992; Li 2010). In Core-annulus structure, there is a dense solids region near the wall and a dilute solids region in the centre of a CFB riser. Particle transportation occurs between the dilute and dense regions. This non-uniform particle distribution results from the existence of particle clusters and greatly influences the aerodynamic characteristics of the CFBs (Grace and Bi 1997; Helland et al. 2007).

At present, there is world-spread effort using computational fluid dynamics (CFD) to solve gas-solids two-phase flows, especially with high performance computing

technology. The Eulerian-Eulerian method with the kinetic theory of granular flow has been widely used to describe gas-solids two-phase flows (Cruz, Steward, and Pugsley 2006; Almuttahar and Taghipour 2008; Wang et al. 2010; Peng, Zhu, and Zhang 2010). In Eulerian-Eulerian method, solids phase is solved using similar structure of Navier-Stokes equation of gas phase. But two items, solids particle pressure and solids shear stress are calculated by granular temperature, which is a theory analogizing to the temperature of gas to describe the intensity of the fluctuation of solids motion (Ding and Gidaspow 1990). Turbulence model for particle phase is employed to describe the mixing of particles at the "cluster" level (Dasgupta, Jackson, and Sundaresan 1994; Hrenya and Sinclair 1997; Cheng et al. 1999; Cheng et al. 2001).

Experiments have shown that the wall has strong influence on particle distributions in CFBs (Savage and Sayed 1984; Craig, Buckholz, and Domoto 1987; Qi, Zhang, and Zhu 2008). In the Jackson and Johnson wall boundary condition (Johnson and Jackson 1987), the specularity coefficient and particle-wall restitution coefficient were introduced to define the wall boundary conditions in numerical simulations. The former describes the roughness of the wall to determine the momentum transfer due to the collision between the particle and wall with the value between 0 for perfectly specular collision and 1 for perfectly diffuse collision. The latter is the coefficient determining the dissipation energy per particle-wall collision. The effect of these two coefficients on the numerical results for solid particle distributions has been studied by several researchers. It was reported that the specularity coefficient strongly affects the core-annulus structure of solids near the wall and particle-wall restitution coefficient only plays a

minor role (Benyahiaa, Syamlala, and O'Brien 2005; Almuttahar and Taghipour 2008; Wang et al. 2010; Li, Grace, and Bi 2010; Lan et al. 2012). Moreover, in CFB simulations, a low specularity coefficient can lead to good numerical results compared to experimental data (Benyahia, Syamlal, and O'Brien 2007; Almuttahar and Taghipour 2008; Wang et al. 2010). However those studies were all carried out by comparing one of the two coefficients at different values when the other one was fixed. The interaction between the two coefficients has not been investigated. Also, for CFBs, the solid particle distribution depends strongly on the particle velocity, but the effect of the wall boundary conditions on the particle velocity has not been investigated. Moreover, as the coefficients defining the physical property of the wall, there is no generality test under different operating conditions

The objective of this study is to investigate the influence of the wall boundary conditions on solid particle distributions with a panoramic viewpoint on the specularity coefficient and particle-wall restitution coefficient. The volume fraction and velocity of solid particles obtained from numerical simulations using different specularity coefficients and particle-wall restitution coefficients are analyzed and compared with available experimental data to validate the numerical model.

3.2 Configuration of the CFB riser

The aerodynamics in a CFB riser was studied experimentally by Li (2010). The CFB system is illustrated in Figure 3.1. The riser is 10m in height with 76.2 mm inner diameter. The gas is supplied from the nozzles on the distributor located at the bottom

of the riser, which is shown on Figure 3.2. It should be noticed that the distributor is not completely axisymmetric. Solid particles from the storage tank are fluidized by the gas from the perforated distributor plate to the top of riser. Due to the height of riser, the two-phase flow can achieve in fully developed flow.

The experiments were conducted by Li (2010) under the operating conditions of superficial velocities of 3 m/s and 5 m/s with solids circulation rates being 50 kg/($m^2 \cdot s$) and 100 kg/($m^2 \cdot s$), respectively. The available experimental data reported by Li (2010) are at 0.11m, 1.02m, 2.39m, 4.78m, 7.32m and 9.61m above the gas distributor of the riser. The radial positions are r/R= 0, 0.316, 0.548 0.707, 0.837 and 0.949, respectively.

3.3 Numerical methods

3.3.1 Governing equations

The simulations of gas-solids two-phase flows in the CFB riser are based on the Eulerian-Eulerian method. The solids phase is treated as a continuum phase solved by mass and momentum transport equations similar to those of the fluid phase. The momentum exchange is coupled by the pressure and interphase exchange coefficient. The solids pressure is calculated in the compressive regime. Due to the collision between particles, granular temperature is introduced to be proportional to the kinetic energy of the particle random motion taking the analogy to the temperature of the gas (Ding and Gidaspow 1990). The governing equations using a k-ε turbulence model for each phase are solved using the finite volume method. The equations are listed as follows:

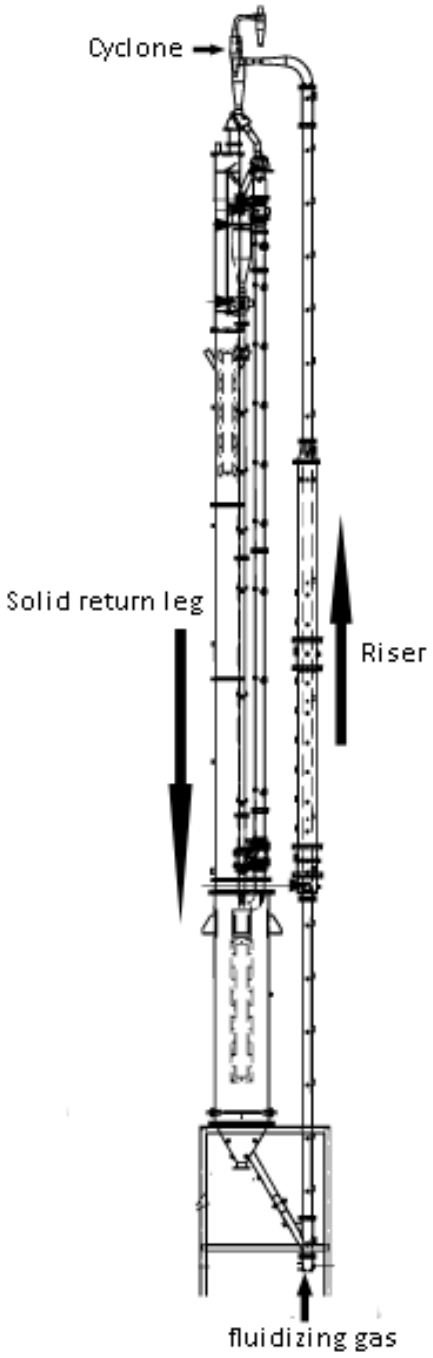

Figure 3.1 Configuration of the CFB system (Li 2010)

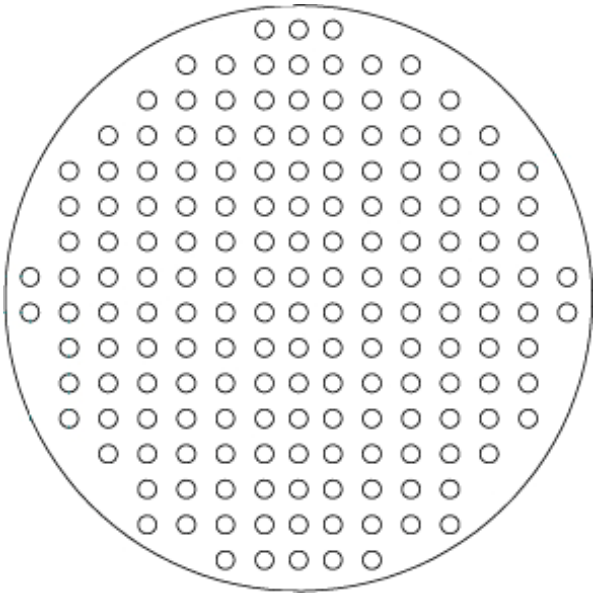

Figure 3.2 Inlet distributor of the riser (Li 2010)

Conservation equation of mass for the gas phase

$$\frac{\partial}{\partial t}\left(\alpha_g \rho_g\right) + \nabla \cdot \left(\alpha_g \rho_g \vec{v}_g\right) = 0 \quad (1)$$

Conservation equation of mass for the solids phase

$$\frac{\partial}{\partial t}\left(\alpha_s \rho_s\right) + \nabla \cdot \left(\alpha_s \rho_s \vec{v}_s\right) = 0 \quad (2)$$

α is volume fraction and $\alpha_g + \alpha_s = 1$

Conservation equation of momentum for the gas phase

$$\frac{\partial}{\partial t}\left(\alpha_g \rho_g \vec{v}_g\right) + \nabla \cdot \left(\alpha_g \rho_g \vec{v}_g \vec{v}_g\right) = -\alpha_g \nabla p + \nabla \cdot \left(\overline{\overline{\tau_{g,m}}} + \overline{\overline{\tau_{g,t}}}\right) + \alpha_g \rho_g \vec{g} + K_{sg}\left(\vec{v}_s - \vec{v}_g\right) \quad (3)$$

where

$$\overline{\overline{\tau_{g,m}}} = \alpha_g \mu_{g,m} \left(\nabla \vec{v}_g + \nabla \vec{v}_g{}^T \right) - \frac{2}{3} \alpha_g \mu_{g,m} \nabla \cdot \vec{v}_g \, \bar{\bar{I}}$$

$$\overline{\overline{\tau_{g,t}}} = -\frac{2}{3} \alpha_g \rho_g k_g \bar{\bar{I}} + \alpha_g \mu_{g,t} \left(\nabla \vec{v}_g + \nabla \vec{v}_g{}^T \right) - \frac{2}{3} \alpha_g \mu_{g,t} \nabla \cdot \vec{v}_g \, \bar{\bar{I}}$$

Conservation equation of momentum for the solids phase

$$\begin{aligned} &\frac{\partial}{\partial t} \left(\alpha_s \rho_s \vec{v}_s \right) + \nabla \cdot \left(\alpha_s \rho_s \vec{v}_s \vec{v}_s \right) \\ &\qquad = -\alpha_s \nabla p - \nabla p_s + \nabla \cdot \left(\overline{\overline{\tau_{s,m}}} + \overline{\overline{\tau_{s,t}}} \right) + \alpha_s \rho_s \vec{s} + K_{gs} \left(\vec{v}_g - \vec{v}_s \right) \end{aligned} \tag{4}$$

where

$$\overline{\overline{\tau_{s,m}}} = \alpha_s \mu_{s,m} \left(\nabla \vec{v}_s + \nabla \vec{v}_s{}^T \right) - \frac{2}{3} \alpha_s \mu_{s,m} \nabla \cdot \vec{v}_s \, \bar{\bar{I}} + \lambda_s \nabla \cdot \vec{v}_s \, \bar{\bar{I}}$$

$$\overline{\overline{\tau_{s,t}}} = -\frac{2}{3} \alpha_s \rho_s k_s \bar{\bar{I}} + \alpha_s \mu_{s,t} \left(\nabla \vec{v}_s + \nabla \vec{v}_s{}^T \right) - \frac{2}{3} \alpha_s \mu_{s,t} \nabla \cdot \vec{v}_s \, \bar{\bar{I}}$$

K is the interphase exchange coefficient and K_{gs}=K_{sg}. Syamlal-O'Brien (Syamlal and O'Brien 1986) model is used in this study, where value is based on measurements of terminal velocity $v_{s,\gamma}$:

$$K_{sg} = \frac{3 \alpha_s \alpha_g \rho_g}{4 v_{s,\gamma}^2 d_s} \left(0.63 + \frac{4.8}{\sqrt{Re_s / v_{s,\gamma}}} \right)^2 \left(\frac{Re_s}{v_{s,\gamma}} \right) \left| \vec{v}_s - \vec{v}_g \right| \tag{5}$$

$$v_{s,\gamma} = 0.5 \left(A - 0.06 Re_s + \sqrt{(0.06 Re_s)^2 + 0.12 Re_s (2B - A) + A^2} \right) \tag{6}$$

where $A=\alpha_g^{4.14}$, $B=0.8\alpha_g^{1.28}$ for $\alpha_g \leq 0.85$ and $B=a_g^{2.65}$ for $\alpha>0.85$ and $\mathrm{Re}_s = \frac{\rho_g d_s |\vec{v}_s - \vec{v}_g|}{\mu_{g,m}}$

The solids pressure and viscosity is related to the granular temperature θ_s based on kinetic theory of granular flow. In the Syamlal-O'Brien model (Syamlal and O'Brien 1986) , it is expressed by

$$p_s = 2\rho_s(1+e_s)\alpha_s^2 g_{s,0}\Theta_s \tag{7}$$

where $g_{s,0}$ is radial distribution function $g_{s,0} = \left[1 - \left(\frac{\alpha_s}{\alpha_{s,max}}\right)^{\frac{1}{3}}\right]^{-1}$.

Solids shear viscosity

$$\mu_s = \mu_{s,m} = \mu_{s,col} + \mu_{s,kin} \tag{8}$$

Collisional viscosity

$$\mu_{s,col} = \frac{4}{5}{\alpha_s}^2 \rho_s d_s g_{s,0}(1+e_{ss})\left(\frac{\Theta_s}{\pi}\right)^{1/2} \tag{9}$$

Kinetic viscosity

$$\mu_{s,kin} = \frac{\alpha_s \rho_s d_s \sqrt{\Theta_s \pi}}{6(3-e_{ss})}\left[1 + \frac{2}{5} g_{s,0}\alpha_s(1+e_{ss})(3e_{ss}-1)\right] \tag{10}$$

Bulk viscosity

$$\lambda_s = \frac{4}{3}\alpha_s \rho_s d_s g_{s,0}(1+e_{ss})\left(\frac{\Theta_s}{\pi}\right)^{1/2} \tag{11}$$

e_{ss} is the particle-particle restitution coefficient taken as empirical value 0.95 (Peng, Zhu, and Zhang 2010).

Granular temperature Θ_s is obtained by solving its transport equation:

$$\begin{aligned}\frac{3}{2}\left[\frac{\partial}{\partial t}(\rho_s \alpha_s \Theta_s) + \nabla\cdot(\rho_s \alpha_s \vec{v}_s\, \Theta_s)\right] \\ = \left[-p_s\bar{\bar{I}} + \left(\bar{\bar{\tau}}_s^{m} + \bar{\bar{\tau}}_s^{t}\right)\right]:\nabla \vec{v}_s + \nabla\cdot(k_{\Theta_s}\nabla\Theta_s) - \gamma_{\Theta_s} + \Phi_{gs}\end{aligned} \tag{12}$$

The diffusion coefficient of energy in Eq. (12) can be obtained by:

$$k_{\Theta_s} = \frac{15\alpha_s\rho_s d_s\sqrt{\Theta_s\pi}}{4(41-33\eta)}\left[1+\frac{12}{5}\eta^2(4\eta-3)\alpha_s g_{s,0} + \frac{16}{15\pi}(41-33\eta)\eta\alpha_s g_{s,0}\right] \tag{13}$$

where $\eta=1/2(1+e_{ss})$.

The collisional dissipation of energy is calculated by:

$$\gamma_{\Theta_s} = \frac{12(1-e_s^2)g_{s,0}}{d_s\sqrt{\pi}}\rho_s {\alpha_s}^2 {\Theta_s}^{3/2} \tag{14}$$

and the energy exchange between two phases is defined as $\phi_{gs}=-K_{gs}\theta_s$ (Gidaspow, Bezburuah, and Ding 1992).

k*-ε *turbulence model for the gas phase

$$\frac{\partial}{\partial t}\left(\alpha_g \rho_g k_g\right) + \nabla \cdot \left(\alpha_g \rho_g \vec{v}_g\, k_g\right) = \nabla \cdot \left(\alpha_g \left(\mu_{g,m} + \frac{\mu_{g,t}}{\sigma_k}\right) \nabla k_g\right) + \left(\alpha_g G_{g,k} - \alpha_g \rho_g \varepsilon_g\right) + K_{sg}\left(C_{sg}\, k_s - C_{gs}\, k_g\right) - K_{sg}\left(\vec{v}_s - \vec{v}_g\right) \frac{\mu_{s,t}}{\alpha_s \sigma_s} \nabla \alpha_s + K_{sg}\left(\vec{v}_s - \vec{v}_g\right) \frac{\mu_{g,t}}{\alpha_g \sigma_g} \nabla \alpha_g \quad (15)$$

$$\frac{\partial}{\partial t}\left(\alpha_g \rho_g \varepsilon_g\right) + \nabla \cdot \left(\alpha_g \rho_g \vec{v}_g\, \varepsilon_g\right) = \nabla \cdot \left(\alpha_g \frac{\mu_{g,t}}{\sigma_\alpha} \nabla \varepsilon_g\right) + \frac{\varepsilon_g}{k_g}\Bigg\{C_{1\varepsilon} \alpha_g G_{g,k} - C_{2\varepsilon} \alpha_g \rho_g \varepsilon_g + C_{3\varepsilon}\Bigg[K_{sg}\left(C_{sg}\, k_s - C_{gs}\, k_g\right) - K_{sg}\left(\vec{v}_s - \vec{v}_g\right) \frac{\mu_{s,t}}{\alpha_s \sigma_s} \nabla \alpha_s + K_{sg}\left(\vec{v}_s - \vec{v}_g\right) \frac{\mu_{g,t}}{\alpha_g \sigma_g} \nabla \alpha_g\Bigg]\Bigg\} \quad (16)$$

where $\mu_{g,t} = \rho_g C_\mu \frac{k_g^2}{\varepsilon_g}$ and $C_\mu = 0.09$.

k*-ε *turbulence model for the solid phase:

$$\frac{\partial}{\partial t}(\alpha_s \rho_s k_s) + \nabla \cdot (\alpha_s \rho_s \vec{v}_s k_s) = \nabla \cdot \left(\alpha_s \left(\mu_{s,m} + \frac{\mu_{s,t}}{\sigma_k}\right) \nabla k_s\right) + (\alpha_s G_{s,k} - \alpha_s \rho_s \varepsilon_s) + K_{gs}(C_{gs} k_g - C_{sg} k_s) - K_{gs}(\vec{v}_g - \vec{v}_s) \frac{\mu_{g,t}}{\alpha_g \sigma_g} \nabla \alpha_g + K_{gs}(\vec{v}_g - \vec{v}_s) \frac{\mu_{s,t}}{\alpha_s \sigma_s} \nabla \alpha_s \quad (17)$$

$$\frac{\partial}{\partial t}(\alpha_s \rho_s \varepsilon_s) + \nabla \cdot (\alpha_s \rho_s \vec{v}_s \varepsilon_s) = \nabla \cdot \left(\alpha_s \frac{\mu_{s,t}}{\sigma_\alpha} \nabla \varepsilon_s\right) + \frac{\varepsilon_s}{k_s} \left\{ C_{1\varepsilon} \alpha_s G_{s,k} - C_{2\varepsilon} \alpha_s \rho_s \varepsilon_s + C_{3\varepsilon} \left[K_{gs}(C_{gs} k_g - C_{sg} k_s) - K_{gs}(\vec{v}_g - \vec{v}_s) \frac{\mu_{g,t}}{\alpha_g \sigma_g} \nabla \alpha_g + K_{gs}(\vec{v}_g - \vec{v}_s) \frac{\mu_{s,t}}{\alpha_s \sigma_s} \nabla \alpha_s \right] \right\} \quad (18)$$

where $\mu_{s,t} = \rho_s C_\mu \frac{k_s^2}{\varepsilon_s}$ and $C_\mu = 0.09$.

3.3.2 Computational domain and boundary conditions

Two-dimensional simulations of the CFB riser shown in Figure 3.1 are carried out in this study. The computational domain is of 10m × 0.0381m according to the dimensions of the CFB riser. The schematic diagram of the computational domain and boundary conditions are shown in Figure 3.3. The boundary conditions at the inlet, outlet and wall are set up according to actual conditions in the riser.

Inlet: the profiles of the velocities of gas and solids, and volume fraction of solids are specified according to the inlet distributor used in the experiment as well as the flow rates of both gas and solid phases. There are 6.5 jets set up along the radius illustrated on Figure 3.4.

Outlet: zero relative pressure is specified.

Wall: for the gas phase, no slip velocity on the wall is used. For the solids phase, the particles can slip on the wall based on the Jackson and Johnson theory (Johnson and Jackson 1987). The shear stress and collision energy are:

$$\tau_s = -\frac{\sqrt{3}\pi\rho_s g_{s,0}\alpha_s\phi\sqrt{\Theta_s}}{6\alpha_{s,max}} \tag{19}$$

$$q_s = \frac{\pi}{6}\sqrt{3}\phi\frac{\alpha_s}{\alpha_{s,max}}\rho_s g_{s,0}\sqrt{\theta_s}\upsilon_{s,w}^2 - \frac{\pi}{4}\sqrt{3}\frac{\alpha_s}{\alpha_{s,max}}\left(1-e_{s,w}^2\right)\rho_s g_{s,0}\theta_s^{\frac{3}{2}} \tag{20}$$

In Eqs. (19) and (20), ϕ is the specularity coefficient and $e_{s,w}$ is the particle-wall restitution coefficient. The second term in Eq. (20) represents the energy loss by collision between particle and wall. . The specularity coefficient describes the roughness of the wall to determine the momentum transfer due to the collision between the particle and wall with the value between 0 for perfectly specular collision and 1 for perfectly diffuse collision. The particle-wall restitution coefficient is the parameter determining the dissipation energy per particle-wall collision. Both of the specularity coefficient and restitution coefficient are empirical to determined by the experiments results (Benyahiaa, Syamlala, and O'Brien 2005; Almuttahar and Taghipour 2008; Wang

et al. 2010; Li, Grace, and Bi 2010; Lan et al. 2012). The operating conditions in numerical simulations are listed in Table 3.1.

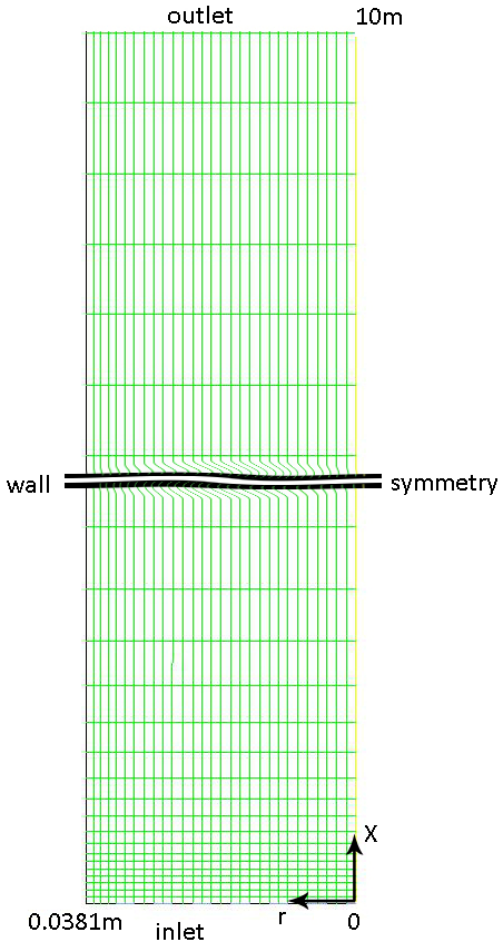

Figure 3.3 Computational domain, mesh and boundary conditions

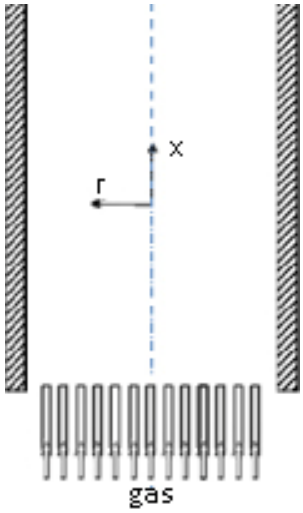

Figure 3.4 Schematic diagram of inlet boundary condition for the gas phase

3.3.3 Solver

The double-precision segregated, implicit formulations and unsteady solver are selected. The phase-coupled SIMPLE algorithm is applied for the pressure-based solver. The discretization scheme for all convection terms is the second-order upwind scheme except for the volume fraction equation where the QUICK scheme is used. A convergence criterion of 10^{-4} for each scaled residual component is specified except for the species fraction, where 10^{-5} is used. The commercial CFD software ANSYS FLUENT 13.0 is used to carry out the simulations with parallel 2.4Ghz nodes.

Table 3.1 Operating conditions and parameters for simulations

Gas density ($\mathrm{kg/m^3}$)	1.225
Gas viscosity ($\mathrm{kg/(m \cdot s)}$)	1.7894×10^{-5}
Particle density ($\mathrm{kg/m^3}$)	1730
Particle diameter ($\mu\mathrm{m}$)	60
Superficial gas velocity ($\mathrm{m/s}$)	3, 5
Particle circulation rate ($\mathrm{kg/(m^2 \cdot s)}$)	50, 100
Particle-particle restitution coefficient	0.95

Particle-wall restitution coefficient	0.95, 0.9, 0.85
Specularity coefficient	0, 0.0001, 0.0002

3.4 Results and discussion

First, to verify whether the solutions reach "steady-state" from the unsteady simulation, the solids volume fraction at outlet of the CFB riser is monitored during the simulation. Figure 3.5 shows that the time-average solids volume fraction at the radial position r/R= 0.5 and the axial position x= 5m. It is clear that the solids volume fraction at that point is nearly unchanged, with oscillation less 1%, after 16 sec of the flow time. Thus, the solutions are considered as steady-state solutions. All the results presented in this study are the steady-state solutions to guarantee the solutions independent of the time.

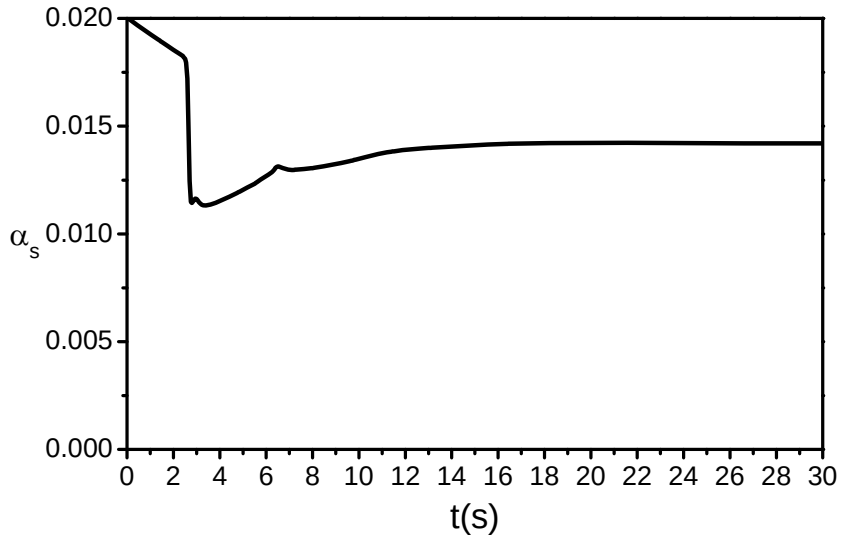

Figure 3.5 Time-average solids volume fraction at r/R= 0.5 and x=5m

3.4.1 Grid independence study

Figure 3.6 shows the results of the grid independence study. It clearly shows that the results using the grids of 12,093, 23,577 and 46,690 cells are almost identical, thus the grid of 12,093 is used in this study.

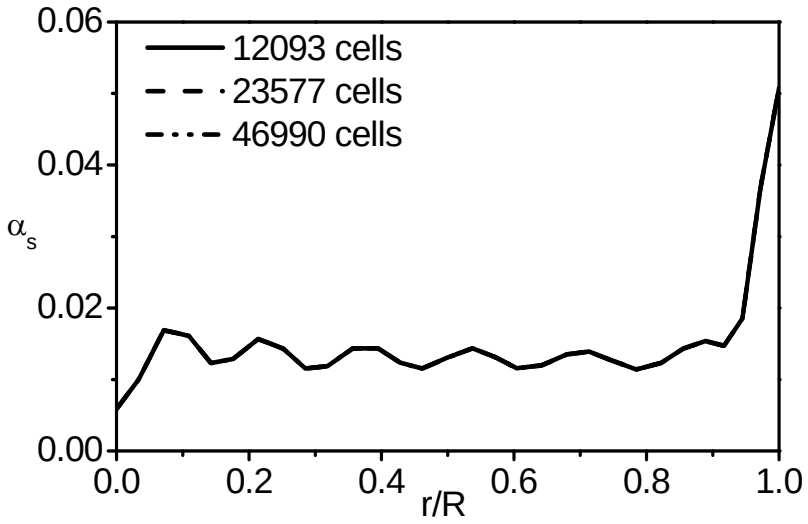

Figure 3.6 Radial profile of the solids volume fraction at x=4.78m with different grids

3.4.2 Time independence study

Figure 3.7 shows the results of numerical simulations using time steps 0.0001s and 0.00001s. From Figure 3.7, it can be seen that the results using the time steps 0.0001s and 0.00001s are almost the same, thus the time step 0.0001s is used in this study.

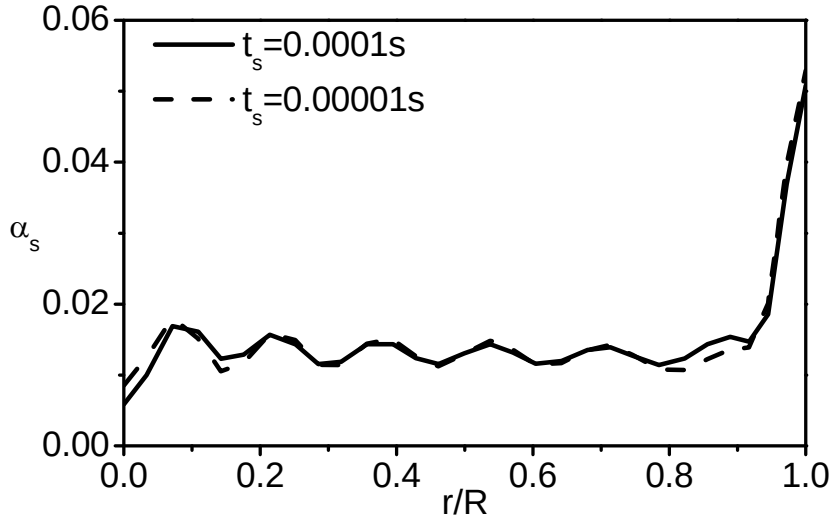

Figure 3.7 Radial profile of the solids volume fraction at x=4.78m with different time steps

3.4.3 The effect of specularity coefficient

Figure 3.8 shows the radial distribution of the solids volume fraction at x=4.78m using different specularity coefficients ϕ when the particle-wall restitution coefficient $e_{s,w}$ is set as 0.95, 0.9 and 0.85, respectively. The obvious core-annulus structure of the solid particle distribution can be seen from the radial profile of the solids volume fraction in the riser. For the same particle-wall restitution coefficient, the change in the specularity coefficient does not have much effect on the solids distributions in the core region. The difference only occurs near the wall. Increasing the specularity coefficient can lead to a decrease in the solids volume fraction near the wall. Zero specularity, which corresponds to free-slip condition on the wall for solid particles, results in the highest volume fraction of solid particles near the wall. When the specularity is 0.0002, the core-annulus structure is changed to that the volume fraction of solid particles at the wall drops, as shown in the Figure 3.8. Figure 3.9 shows the axial distribution of the

solids volume fraction at the wall using different specularity coefficients when the particle-wall restitution coefficients are 0.95, 0.9 and 0.85, respectively. It can be seen that the solids volume fraction at the wall decreases along the axial direction for all values of the specularity coefficients and particle-wall restitution coefficients tested here. It also can be seen that the trend of the effect of the specularity coefficients on the solids distribution is consistent, i.e. a higher specularity coefficient results in a lower solids volume fraction at the wall for a given particle-wall restitution coefficient and the decrease in the solids volume fraction at the wall along the axial direction is faster when the specularity coefficient is higher. So, the difference in solids volume fractions at the wall using different specularity coefficients becomes larger along the axial direction for a given particle-wall restitution coefficient. Based on Eq. (19), higher specularity coefficient means higher wall shear stress, resulting in higher flow resistance for the particles to move upward. Therefore, the solids volume fraction at the wall decreases faster along the axial direction when the specularity coefficient is higher as shown in Figure 3.9. In addition, when the particle-wall restitution coefficient decreases, the difference in solids volume fractions at the wall using different specularity coefficients becomes smaller. Thus, the specularіy coefficient has a strong effect on the solid particle distribution near the wall and this effect becomes weaker when the particle-wall restitution coefficient decreases. The decrease in the particle-wall restitution coefficient means the increase in the energy loss by collision between the particle and the wall based on Eq. (20). So, the particle kinetic energy will decrease and the specularity

coefficient will have less effect on the particle flow when the particle-wall restitution coefficient is low.

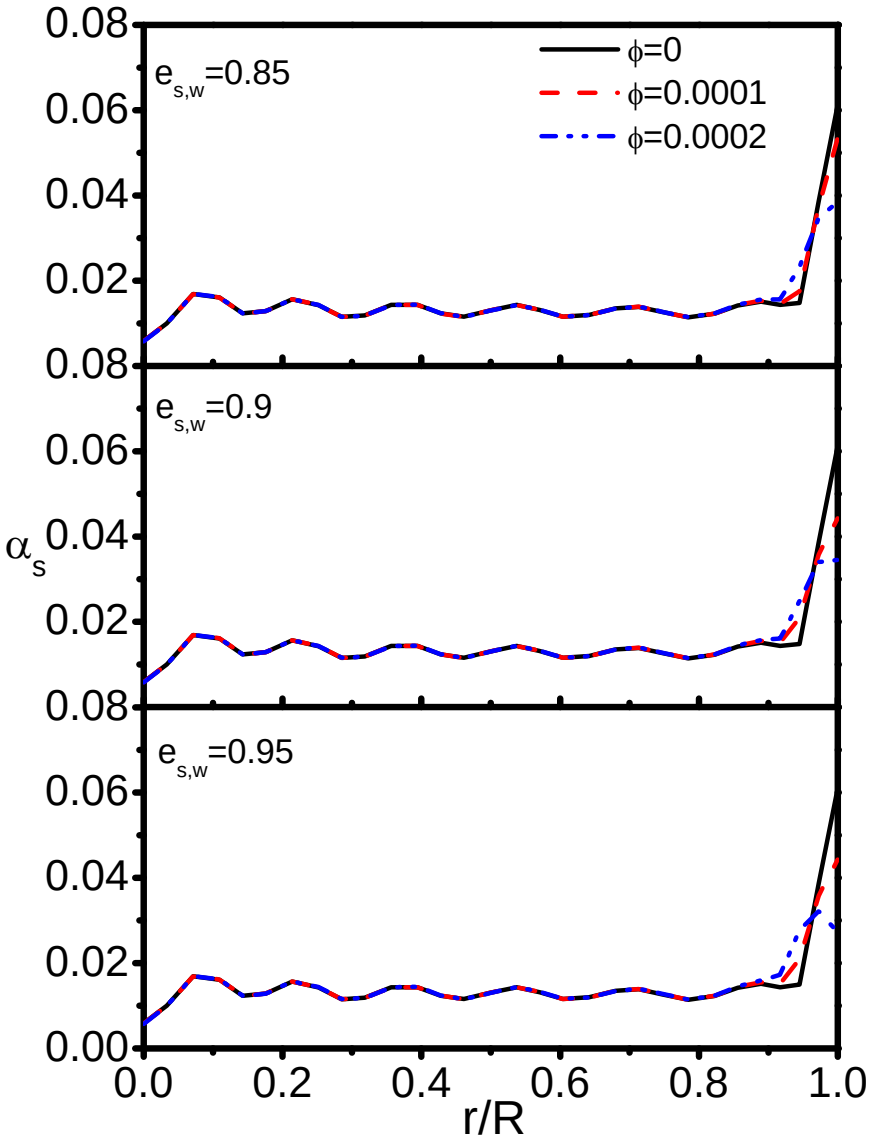

Figure 3.8 Radial profile of solids volume fraction at x=4.78m with different specularity coefficients.

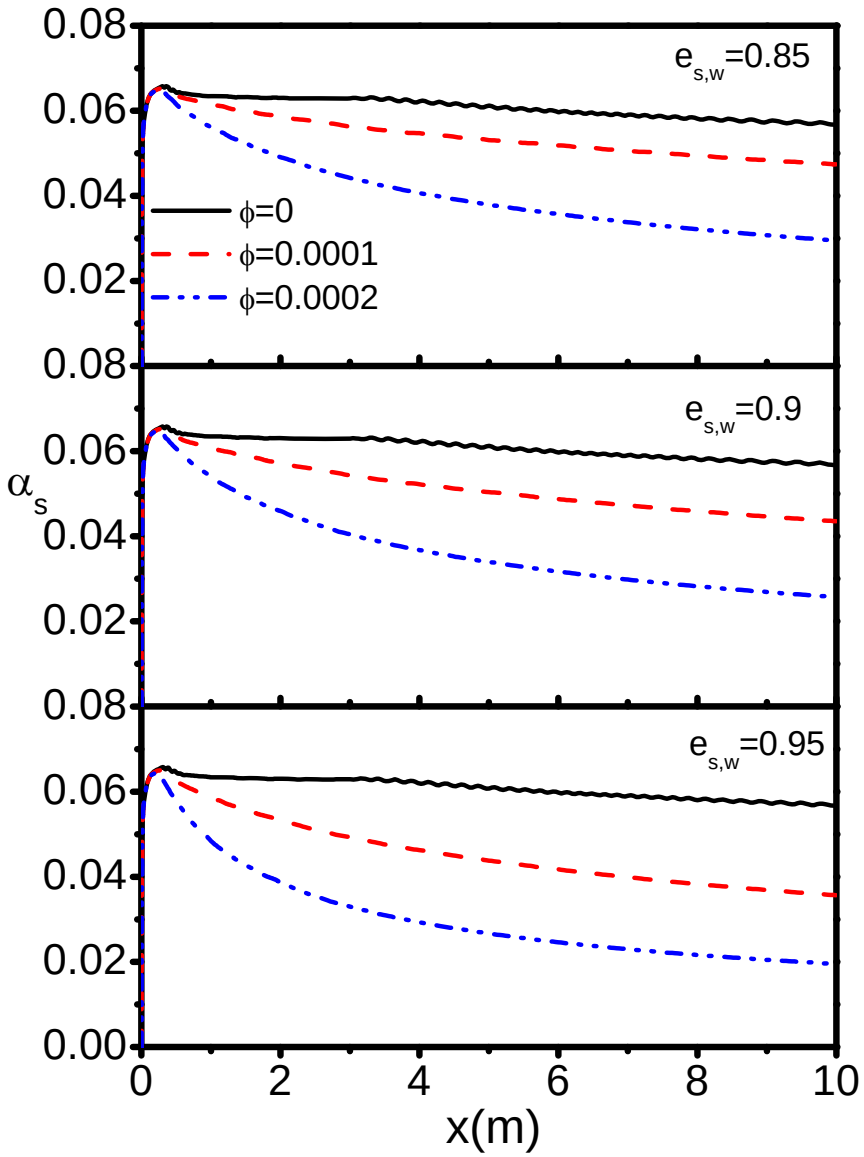

Figure 3.9 Axial profile of the solids volume fraction at the wall with different specularity coefficients.

3.4.4 The effect of particle-wall restitution coefficient

Figures 3.10 and 3.11 show the radial profiles of the solids volume fraction at x=4.78m and axial profiles of the solids volume fraction at the wall using different particle-wall restitution coefficients when specularity coefficients are 0, 0.0001 and 0.0002,

respectively. As reported by Almuttahar and Taghipour (2008), when the specularity coefficient is 0, the particle–wall restitution coefficient only plays a minor role on the solids distribution. Moreover, its effect on the solids distribution in the riser axial direction can be ignored. It can also be seen from Figures 3.10 and 3.11 that the particle-wall restitution coefficient has no effect on the solids distribution in both radial and axial directions when the specularity coefficient is 0. However, when the specularity coefficient increases, the particle-wall restitution coefficient will start affecting particle distributions. When the specularіy coefficients are 0.0001 and 0.0002, a lower particle-wall restitution coefficient results in higher solids volume fraction near the wall, which can be seen from both Figures 3.10 and 3.11. This is because the fact that a lower particle-wall restitution coefficient means higher energy loss by collision between the particle and the wall based on Eq. (20). So, particles have less energy to move away from the wall after the collision, which results in a higher solids volume fraction at the wall. Same as the specularity coefficient, the particle–wall restitution coefficient does not affect the radial profile of the solids volume fraction in the centre region of the riser. In addition, the effect of this restitution coefficient becomes more obvious as the specularity coefficient increases as shown in Figures 3.10 and 3.11. And also, at a higher axial location in the riser, the difference in the results using different particle-wall restitution coefficients becomes bigger as shown in Figure 3.11. Thus, the effect of the particle-wall restitution coefficient on the solids distribution near the wall will be weak with the decrease in the specularity coefficient, and it is so weak that can be ignored when the specularity coefficient is 0. Through comparing the two different coefficients,

it also can be seen that the predicted solids volume fraction is more sensitive to the specularity coefficient than the particle-wall restitution coefficient.

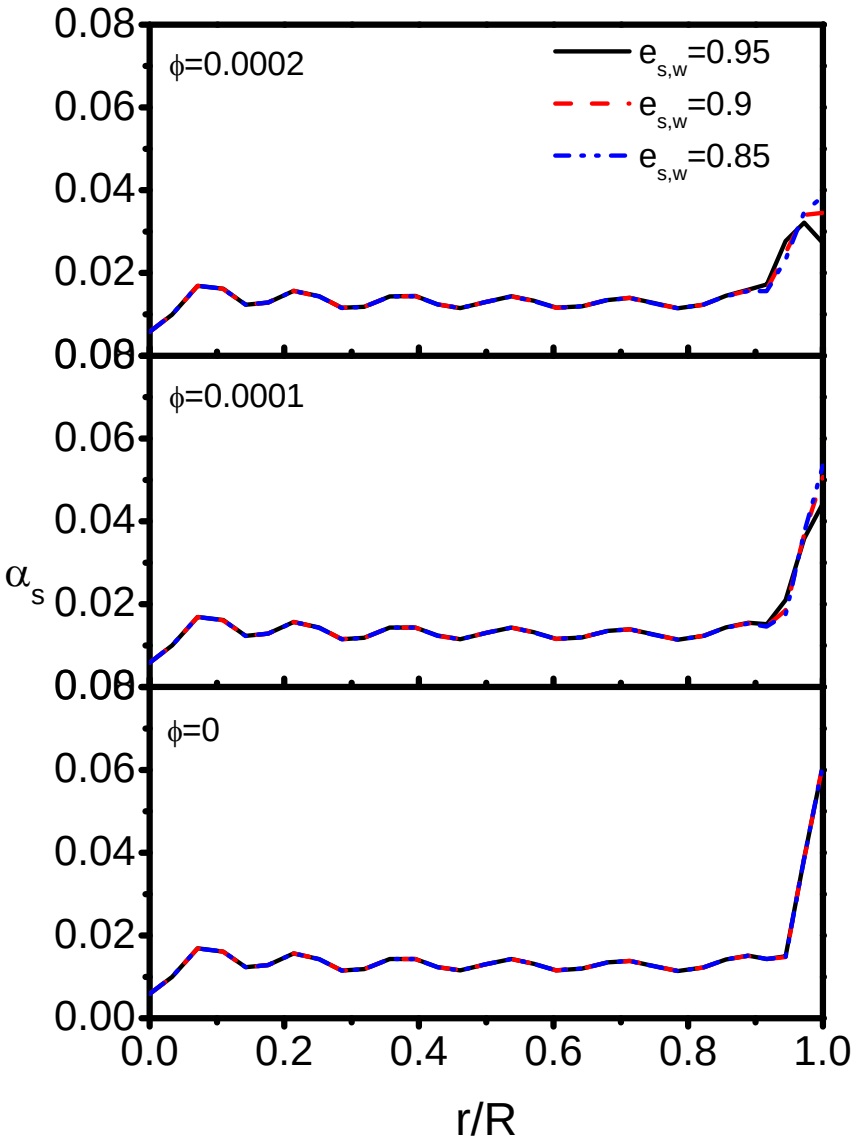

Figure 3.10 Radial profile of the solids volume fraction at x=4.78m with different particle-wall restitution coefficients

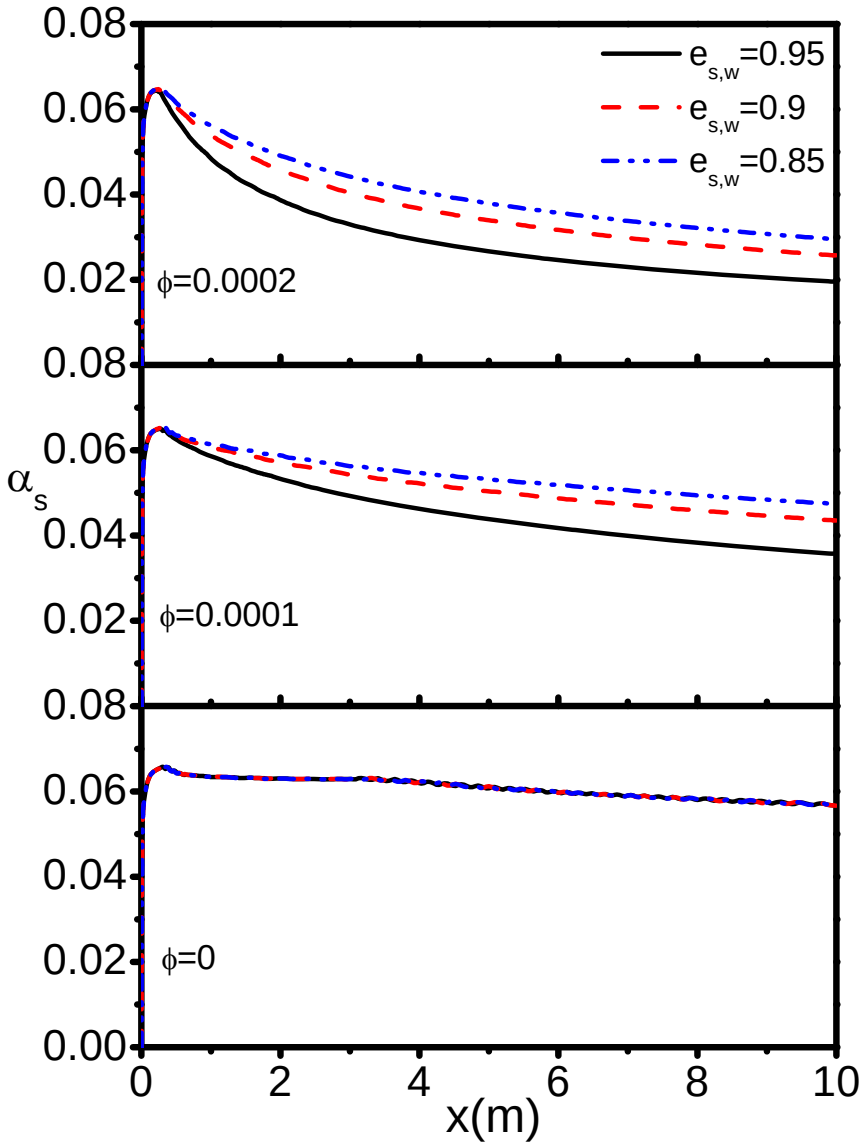

Figure 3.11 Axial profile of the solids volume fraction at the wall with different particle-wall restitution coefficients.

3.4.5 Lateral velocity of solid particles

Both Almuttahar and Taghipour (2008) and Benyahia et al (2007) indicated the specularity coefficient and particle-wall restitution coefficient do not affect the axial velocity of particles. Nonetheless, in a typical CFB riser, the inlet gas distributor has numbers of jets, so the lateral velocity cannot be neglected due to the jet effect. The

lateral velocity is zero on the wall, so that particle cannot pass through the wall. Tables 3.2 and 3.3 show the lateral velocity and solids volume fraction at the radial position of r/R=0.99764, which is extremely close to wall, and the axial position of x=2m in the riser. The solids velocity at this point can be considered as the velocity contributed by the particle-wall collision. It should be noticed that the solids lateral velocity at this point is negative for all cases, which means the particles move away from the wall. From Table 3.2, it can be seen when the specularity coefficient is 0, the lateral velocity does not change with the particle-wall restitution coefficient, which is consistent with the results shown in Figures 3.10 and 3.11 that the particle-wall restitution coefficient has no effect on the solids flow when the specularity coefficient is 0. However, the solids lateral velocity changes with the particle-wall restitution coefficient when the specularity coefficient increases. And the lateral velocity increases when the specularity coefficient or particle-wall restitution coefficient increases. This is understandable. Higher specularity coefficient means higher wall shear stress, resulting in higher flow resistance for the particles to move upward. Therefore, the lateral velocity increases, resulting in a decrease in the solids volume fraction near the wall as shown in Figure 3.9 and Table 3.3. Also, higher particle-wall restitution coefficient means lower energy loss by collision between the particle and the wall. So, particles have more energy to move away from the wall after the collision, which results in a higher solids lateral velocity and lower solids volume fraction rear the wall as shown in Figure 3.11 and Table 3.3. The correlation between the solid particle lateral velocity and volume fraction is that the lateral velocity is inversely proportional to the volume fraction. The larger the lateral

velocity is, the particle has more chance to flow away from the wall which leads few particles near the wall, so the volume fraction is lower.

Table 3.2 Solids lateral velocity near the wall from different specularity coefficients and particle-wall restitution coefficients

Solids lateral velocity ϕ / $e_{s,w}$	0	0.0001	0.0002
0.95	-0.000086	-0.000313	-0.000828
0.9	-0.000086	-0.000217	-0.000531
0.85	-0.000086	-0.000182	-0.000417

Table 3.3 Solids volume fraction near the wall from different specularity coefficients and particle-wall restitution coefficients

Solids volume fraction ϕ / $e_{s,w}$	0	0.0001	0.0002
0.95	0.063054	0.053299	0.038746
0.9	0.063046	0.057283	0.045963
0.85	0.063039	0.058835	0.049139

3.4.6 The effect of operating conditions

After comparing numerical results using different values of these two coefficients with the experimental data (Li 2010), it is found that the specularity coefficient 0.0001 and particle-wall restitution coefficient 0.9 give the best agreement between the numerical results and experimental data. As those coefficients determining the physical properties between particles and wall, the specularity coefficient and particle-wall restitution coefficient have to be verified for the generality under different operating conditions.

Figure 3.12 presents the comparison between the numerical results using the specularity coefficient 0.0001 and particle-wall restitution coefficient 0.9 and experimental data for the radial profiles of the solids volume fraction in the riser with different gas superficial velocities and solid particles circulation rates. It clearly shows the core annulus structure in the whole riser which is dilute in the centre and dense near the wall. The fluctuations of the solids volume fraction in the core region is due to the air jets at the inlet gas distributor and the details about the air jet effect are given in Appendix. The solids volume fraction in the core region does not change much along the axial direction while it decreases near the wall in the axial direction. Comparing the results from both numerical simulations and experiments under different operating conditions, it is found that the solids volume fraction increases in the riser with the increase in the solids flux or decrease in the gas velocity. In general, the agreement between the numerical results and experimental data is good. The agreement is better when the gas flow rate is higher. Also, the agreement is good in the upper region of the riser. However, near the inlet, the simulation does not match with the experiment well. This could be contributed by the high gradient of the velocity and the error of both numerical and experimental methods.

The comparison for the radial profiles of the solids velocity at different axial locations under different operating conditions is shown in Figure 3.13. The solids velocity decreases close to wall and the gradient is very high near the wall. The solids velocity increases significantly with the increase in the gas velocity, but the solids circulation rate only plays a minor role on the solids velocity, which can be seen in both experimental

and numerical results. And near the wall, the solids velocity is close to zero or even negative which is called back mixing due to gravity (Zhu et al. 1995). Similar to the solid holdup, the agreement between the numerical results and experimental data is generally good. However, larger discrepancy occurs near the inlet.

The specularity coefficient and particle-wall restitution coefficient are both empirically determined parameters. The evaluations of them, therefore are based on the experiments under different operating conditions to ensure the generality. The closest sampling position to the wall in experiment is only at r/R=0.949, but for CFB simulations, the numerical results show a very large gradient in the radial profile between 0.949 and 1, which can be tuned by these two coefficient. Thus for both numerical and experimental methods, the region near the wall should be still investigated precisely.

3.5 Conclusions

The 2D simulations of the gas-solids flow in a circulating fluidized bed riser have been carried out using the Eulerian-Eulerian method and kinetic theory of granular flow. The wall boundary condition is defined based on the Jackson and Johnson wall theory. The solid particle volume fractions obtained using different specularity coefficients and particle-wall restitution coefficients are compared. The results show that the specularity coefficient has a strong effect on the solid particle distribution near the wall and the effect becomes weaker with the increase in the particle-wall restitution coefficient. The particle-wall restitution coefficient has less effect on solid particle distribution near the wall than that of specularity coefficient and the effect becomes less when the

specularity coefficient decreases. In addition, the wall boundary condition affects the lateral velocity of the solid particles near the wall, which affects the solids volume fraction near the wall. By comparing with experimental data, the appropriate specularity coefficient and particle-wall restitution coefficient have been proposed. However the experimental results in the region near the wall are needed to further validate the specularity and particle-wall restitution coefficients.

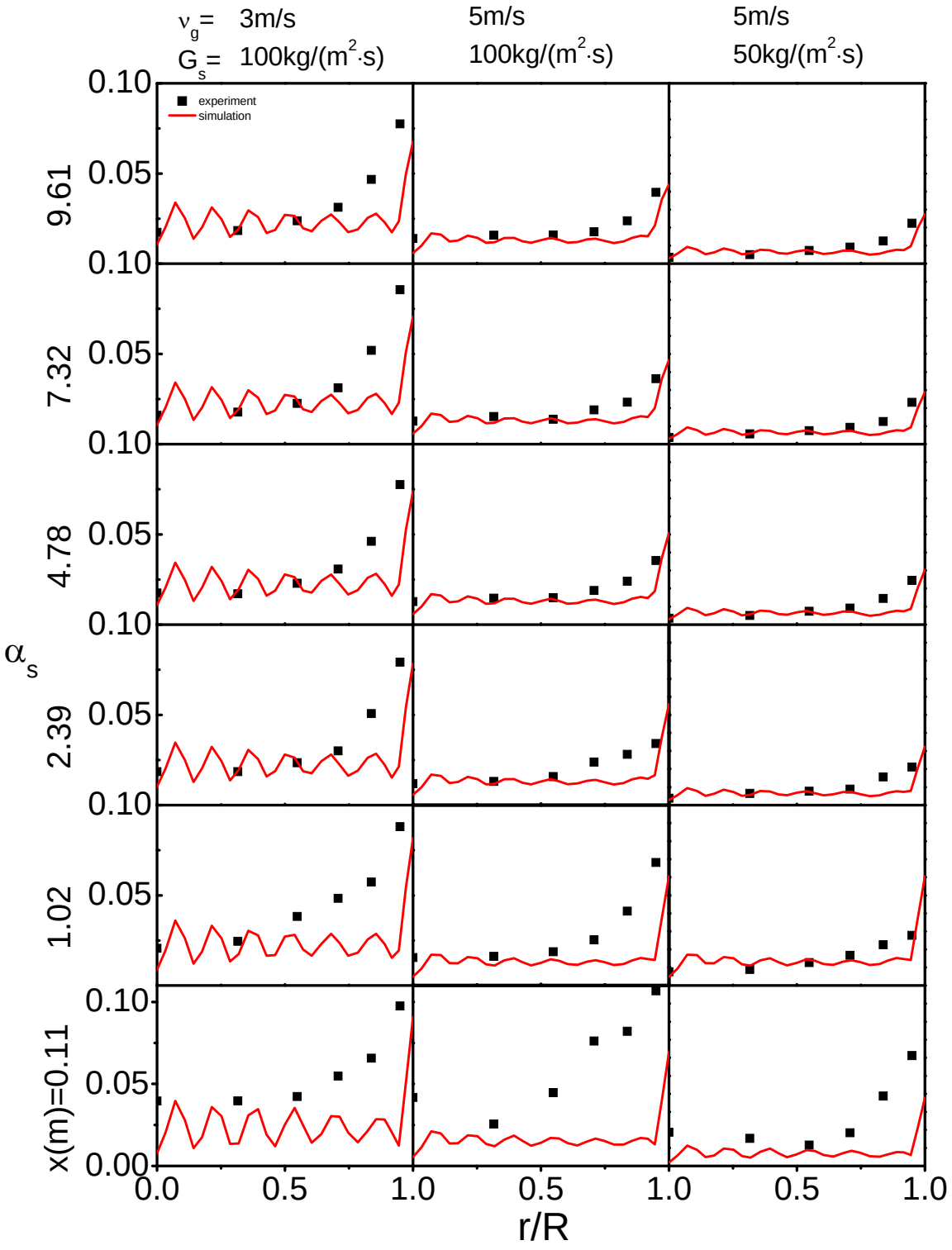

Figure 3.12 Solids volume fraction in radial profile under different operating conditions

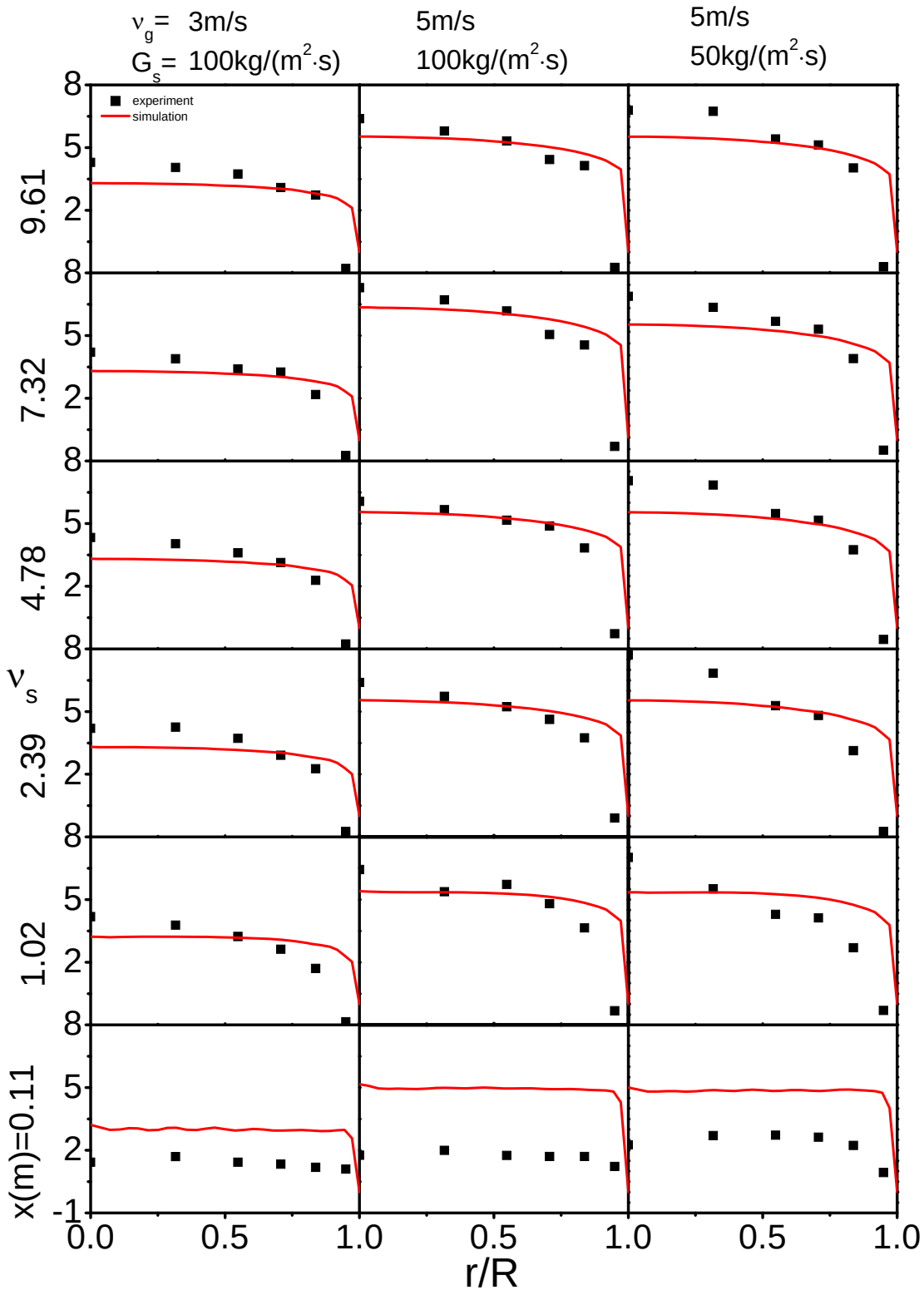

Figure 3.13 Particle velocity in radial profile under different operating conditions

Nomenclature

C_μ = turbulence constant, dimensionless
$C_{1\varepsilon}$ = turbulence constant, dimensionless
$C_{2\varepsilon}$ = turbulence constant, dimensionless
$C_{3\varepsilon}$ = turbulence constant, dimensionless
d = diameter, m
e= restitution coefficient, dimensionless
G_s = solids circulation rate, kg/m^2s
g = gravity, m/s^2
$g_{s,0}$ = radial distribution function, dimensionless
I = unit matrix, dimensionless
K = interphase exchange coefficient, kg/m^3s
k = turbulence kinetic energy, m^2/s^2
$k_{\theta s}$= diffusion coefficient of energy, kg/ms
p = pressure, Pa
q = collision energy, kg/s^3
R= radius of the riser, m
r = radial coordinate, m
Re = Reynolds number, dimensionless
v = velocity, m/s
x = axial coordinate, m

Greek symbols

α = volume fraction, dimensionless
γ = collision dissipation of energy, kg/ms^3
ε = turbulence dissipation rate, m2/s^3
θ = granular temperature, m2/s^2
λ = bulk viscosity, kg/ms
μ = viscosity, kg/ms
ρ = density, kg/m^3
τ = stress tensor, Pa
Φ = energy exchange coefficient, kg/ms^3
ϕ = specularity coefficient, dimensionless

Subscripts

g = gas phase
s = solids phase
m = molecular
t = turbulence
w= wall

References

Almuttahar, A., & Taghipour, F. (2008). Computational fluid dynamics of high density circulating fluidized bed riser: Study of modeling parameters. *Powder Technology , 185*, pp. 11-23.

Benyahia, S., Syamlal, M., & O'Brien, T. J. (2007). Study of the ability of multiphase continuum models to predict core-annulus flow. *AIChE Journal , 53* (10), pp. 2549-2568.

Benyahiaa, S., Syamlala, M., & O'Brien, T. J. (2005). Evaluation of boundary conditions used to model dilute, turbulent gas/solids flows in a pipe. *Powder Technology , 156*, pp. 62 – 72.

Cheng, Y., Guo, Y., Wei, F., & Jin, Y. (2001). CFD simulation of hydrodynamics in the entrance region of a downer. *Chem. Eng. Sci. , 56* (4), pp. 1687–1696.

Cheng, Y., Guo, Y., Wei, F., Jin, Y., & Lin, W. (1999). Modeling the hydrodynamics of downer reactors based on kinetic theory. *Chem. Eng. Sci. , 54* (13-14), pp. 2019-2927.

Craig, K., Buckholz, R. H., & Domoto, G. (1987). Effect of shear surface boundaries on stress for shearing flow of dry metal powders — an experimental-study. *Journal of Tribology-Transactions of the ASME , 109* (2), pp. 232–237.

Cruz, E., Steward, F. R., & Pugsley, T. (2006). New closure models for CFD modeling of high-density circulating fluidized beds. *Powder Technology , 169*, pp. 115–122.

Dasgupta, S., Jackson, R., & Sundaresan, S. (1994). Turbulent gas-particle flow in vertical risers. *AICHE Journal , 40* (2), pp. 215-228.

Ding, J., & Gidaspow, D. (1990). A bubbling fluidization model using kinetic theory of granular flow. *AIChE Journal , 36* (4), pp. 523–538.

Gidaspow, D., Bezburuah, R., & Ding, J. (1992). Hydrodynamics of circulating fluidized beds, kinetic theory approach. In *Fluidization VII: Proceedings of the 7th Engineering Foundation Conference on Fluidization.* 75-82.

Grace, J. R. (1990). High-velocity fluidized bed reactors. *Chemical Engineering Science , 45* (8), pp. 1953–1966.

Grace, J. R., & Bi, H. (1997). Introduction to circulating fluidized beds. In J. R. Grace, A. Avidan, & T. Knowlton, *Circulating fluidized beds* (pp. 1-19). New York: Engineering Foundation.

Helland, E., Bournot, H., Occelli, R., & Tadrist, L. (2007). Drag reduction and cluster formation in a circulating fluidised bed. *Chemical Engineering Science , 62* (1-2), pp. 148-158.

Hrenya, C. M., & Sinclair, J. L. (1997). Effects of particle-phase turbulence in gas-solid flows. *AIChE Journal , 43* (4), pp. 853-869.

Huang, W., Yan, A., & Zhu, J. (2007). Hydrodynamics and flow development in a 15.1 m circulating fluidized bed riser. *Chem. Eng. & Technol , 30* (4), pp. 460-466.

Huang, W., Zhu, J., & Parssinen, J. H. (2006). Comprehensive study on solids acceleration length in a long CFB riser. *29* (10), 1197-1204.

Johnson, P. C., & Jackson, R. (1987). Frictional-collisional constitutive relations for granular materials, with application to plane shearing. *J. Fluid Mech. , 176*, pp. 67-93.

Lan, X. Y., Xu, C. M., Gao, J. S., & Al-Dahhan, M. (2012). Influence of solid-phase wall boundary condition on CFD simulation of spouted beds. *Chemical Engineering Science , 69*, pp. 419-430.

Li, D. B. (2010). *Investigation of circulating fluizied bed riser and downer reactor performance for catalytic ozone decompostion.* Phd Thesis, Univ. of Western Onatario.

Li, T. W., Grace, J., & Bi, X. T. (2010). Study of wall boundary condition in numerical simulations of bubbling fluidized beds. *Powder Technology , 203*, pp. 447-457.

Miller, A., & Gidaspow, D. (1992). Dense, vertical gas–solids flow in a pipe. *AIChE J. , 38*, pp. 1801-1813.

Peng, B. T., Zhu, J., & Zhang, C. (2010). Numerical study on the effect of the air jets at the inlet distributor in the gas-solids circulating fluidized-bed risers. *Ind. Eng. Chem. Res. , 49*, pp. 5310–5322.

Qi, X. B., Zhang, H., & Zhu, J. (2008). Friction between gas–solid flow and circulating fluidized bed downer wall. *Chemical Engineering Journal , 142*, pp. 318–326.

Qi, X., Huang, W., Pan, Y., Zhu, J., & Shi, Y. (2003). Investigation on solids concentration and core-annulus flow structure in circulating fluidized bed risers. *J. Sichuan Univ. , 35* (1), pp. 43-47.

Reh, L. (1999). Challenges of circulating fluid-bed reactors in energy and raw materials industries. *Chemical Engineering Science , 54* (22), pp. 5359–5368.

Savage, S. B., & Sayed, M. (1984). Stresses developed by dry cohesionless granular-materials sheared in an annular shear cell. *Journal of Fluid Mechanics , 142*, pp. 391–430.

Syamlal, M., & O'Brien, T. (1986). Computer simulation of bubbles in a fluidized bed. *AIChE Symposium Series , 85*, pp. 22-31.

Wang, X. F., Jin, B. S., Zhong, W. Q., & Xiao, R. (2010). Modeling on the hydrodynamics of a high-flux circulating fluidized bed with geldart group a particles by kinetic theory of granular flow. *Energy Fuels , 24*, pp. 1242–1259.

Yan, A., & Zhu, J. (2004). Scale-up effect of riser reactors (1) axial and radial solids concentration distribution and flow development. *Ind & Eng Chem Res , 43* (19), pp. 5810-5819.

Zhu, J. X., & Cheng, Y. (2005). Fluidized-Bed Reactors and Applications. In C. Crowe (Ed.), *Multiphase Flow Handbook* (pp. 5.55-5.93). New York: CRC Press.

Zhu, J. X., Yu, Z. Q., Jin, Y., Grace, J. R., & Issangya, A. (1995). Cocurrent downflow circulating fluidized bed (downer) reactors - A state of the art review. *The Canadian Journal of Chemical Engineering , 73* (5), pp. 662–677.

Chapter 4.

4 Two dimensional simulation of catalytic ozone decomposition reaction in a gas-solids circulating fluidized bed riser

4.1 Introduction

Fluidization is a process that fine solid particles are transformed from a fixed solid-like state into a fluid-like state through contacting with a flowing gas or liquid. A gas-solids circulating fluidized bed (CFB) is a reactor device based on the fluidization phenomenon between gas and particles, which can be applied to implement a variety of multiphase chemical reactions. It is well know that CFBs have higher gas-solids contact efficiency, reduced axial dispersion for both gas and solids phases and higher gas-solids throughput (Grace 1990; Reh 1999; Zhu and Cheng 2005).

The aerodynamic study is important to improve CFB designs. A non-uniform radial distribution of the solid particles has been found in CFB risers, which is called core-annulus structure (Qi et al. 2003; Yan and Zhu 2004; Huang, Zhu, and Parssinen 2006; Huang, Yan, and Zhu 2007; Miller and Gidaspow 1992; Li 2010). Core-annulus structure of solid particles in the radial profile represents a dense solids region near the wall and a dilute solids region in the centre of the CFB. Particle transportation occurs between the dilute and the dense regions. This non-uniform particle distribution results from the existence of particle clusters and greatly influences the aerodynamic characteristics of the CFBs (Grace and Bi 1997; Helland et al. 2007).

To study the characteristics of gas-solids reactions in a CFB, catalytic ozone decomposition is often used as the model reaction in last two decades (Kagawa et al. 1990; Jiang et al. 1990; Jiang et al. 1991; Bi et al. 1992; Ouyang, Lin, and Potter 1993; Ouyang, Li, and Potter 1995; Bolland and Nicolai 2001; Li 2010). During a fluidization process in a CFB, catalytic decomposition of ozone into diatomic oxygen requires very low concentration of the ozone so that the gas density and temperature changes caused by the reaction in the CFB can be neglected. In addition, the catalytic ozone decomposition reaction has an easily measurable first-order reaction rate at ambient temperature. Moreover, ozone detection technology is effective using fairly simple methods (Syamlal and O'Brien 2003). Thus, all these advantages make catalytic ozone decomposition the most widespread model reaction for the study of the characteristics of gas-solids reactions in CFBs.

With the high pace of technology development in high-performance computers, there is a worldspread effort using computational fluid dynamics (CFD) to solve gas-solids two-phase flows. The Eulerian-Eulerian method with kinetic theory of granular flow has been widely used to solve the solid particle phase (Cruz, Steward, and Pugsley 2006; Almuttahar and Taghipour 2008; Wang et al. 2010; Peng, Zhu, and Zhang 2010). Turbulence model for the particle phase is used to describe the mixing of particles at the “cluster” level (Dasgupta, Jackson, and Sundaresan 1994; Hrenya and Sinclair 1997; Cheng et al. 1999; Cheng et al. 2001).

Very few works have been reported in the literature on the coupling between detailed aerodynamic modeling and chemical reactions in CFB systems. Therdthianwong et al (2003) modeled 2D ozone decomposition reaction in a CFB riser, but the predicted solids distribution was not the typical core-annulus structure and the ozone concentration did not match well with the particle distribution. Although Hansen et al (2004) and Dong et al (2008) reported the results about the simulation of ozone decomposition in a gas-solids CFB riser with the kinetic theory of granular flow with a good agreement with experiments. However, the numerical solutions of ozone concentration and solids volume fraction presented oscillated in a range between 5% and 50% of the average value, which seems the simulation was not converged, although it matched with the experimental data well at certain flow time. Moreover, the reaction rate equation was not with respect to particles surface area, which can not reflect the effect of the particle sizes in the reaction.

Therefore, the objectives of this study are (1) to develop a completed CFD model for catalytic ozone decomposition in a CFB riser using the Eulerain-Eulerian method and kinetic theory of granular flow; (2) to validate the generality of the proposed CFD model by comparing with the experimental data under different operating conditions. In addition, the effect of the particle size on the reaction rate will also be also investigated.

4.2 Configuration of the CFB riser

The CFB riser used in this study is from the previous work by Li (2010), where the catalytic ozone decomposition experiment in CFB riser was carried out. The CFB system

is illustrated in Figure 4.1. The riser is 10m in height with 76.2 mm inner diameter. The air contained about 20 ppm ozone is supplied from the nozzles on the distributor located at the bottom of the riser, which are shown on Figure 4.2. It should be noticed that the distributor is not axisymmetric. Solid particles from the storage tank are fluidized by gas form the perforated distributor plate to the top of riser. Due to the height of riser, the two-phase flow can achieve in fully developed flow.

The experiments were conducted by Li (2010) under the operating conditions of superficial velocities of 3 m/s and 5 m/s with solids circulation rates being 50 kg/($m^2 \cdot s$) and 100 kg/($m^2 \cdot s$), respectively. The available experimental data reported by Li (2010) are at 0.11m, 1.02m, 2.39m, 4.78m, 7.32m and 9.61m above the gas distributor of the riser. The radial positions are r/R= 0, 0.316, 0.548 0.707, 0.837 and 0.949, respectively.

4.3 Numerical model

4.3.1 Governing equations

The simulations of gas-solids two-phase flow in the CFB riser are based on the Eulerian-Eulerian method. Solids phase is treated as a continuum phase solved by mass and momentum transport equations similar to those of fluid phase. The momentum exchange is coupled by pressure and interphase exchange coefficient. The solids pressure is calculated in the compressive regime. Due to collision between particles, granular temperature is introduced to be proportional to the kinetic energy of the particles random motion taking the analogy to the temperature of gas (Ding and

Gidaspow 1990). The governing equations using a k-ε turbulence model for each phase are solved using the finite volume method. The equations are listed as follows:

Conservation equation of mass for the gas phase

$$\frac{\partial}{\partial t}\left(\alpha_g \rho_g\right) + \nabla \cdot \left(\alpha_g \rho_g \vec{v}_g\right) = 0 \quad (1)$$

Conservation equation of mass for the solids phase

$$\frac{\partial}{\partial t}\left(\alpha_s \rho_s\right) + \nabla \cdot \left(\alpha_s \rho_s \vec{v}_s\right) = 0 \quad (2)$$

α is volume fraction and $\alpha_g + \alpha_s = 1$

Conservation equation of momentum for the gas phase

$$\frac{\partial}{\partial t}\left(\alpha_g \rho_g \vec{v}_g\right) + \nabla \cdot \left(\alpha_g \rho_g \vec{v}_g \vec{v}_g\right) = -\alpha_g \nabla p + \nabla \cdot \left(\overline{\overline{\tau_{g,m}}} + \overline{\overline{\tau_{g,t}}}\right) + \alpha_g \rho_g \vec{g} + K_{sg}\left(\vec{v}_s - \vec{v}_g\right) \quad (3)$$

where

$$\overline{\overline{\tau_{g,m}}} = \alpha_g \mu_{g,m}\left(\nabla \vec{v}_g + \nabla \vec{v}_g{}^T\right) - \frac{2}{3}\alpha_g \mu_{g,m} \nabla \cdot \vec{v}_g \, \bar{\bar{I}}$$

$$\overline{\overline{\tau_{g,t}}} = -\frac{2}{3}\alpha_g \rho_g k_g \bar{\bar{I}} + \alpha_g \mu_{g,t}\left(\nabla \vec{v}_g + \nabla \vec{v}_g{}^T\right) - \frac{2}{3}\alpha_g \mu_{g,t} \nabla \cdot \vec{v}_g \, \bar{\bar{I}}$$

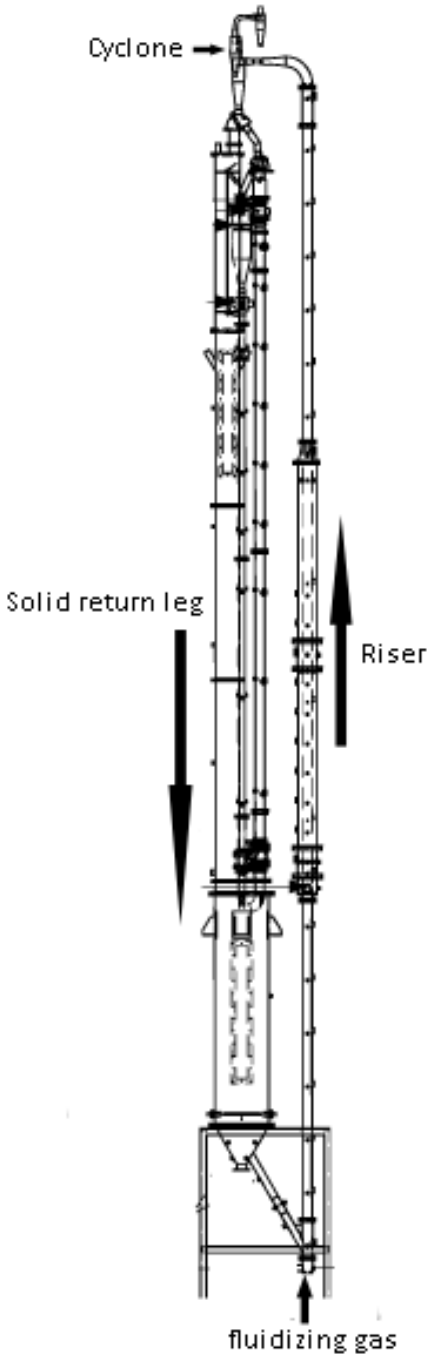

Figure 4.1 Configuration of the CFB system (Li 2010)

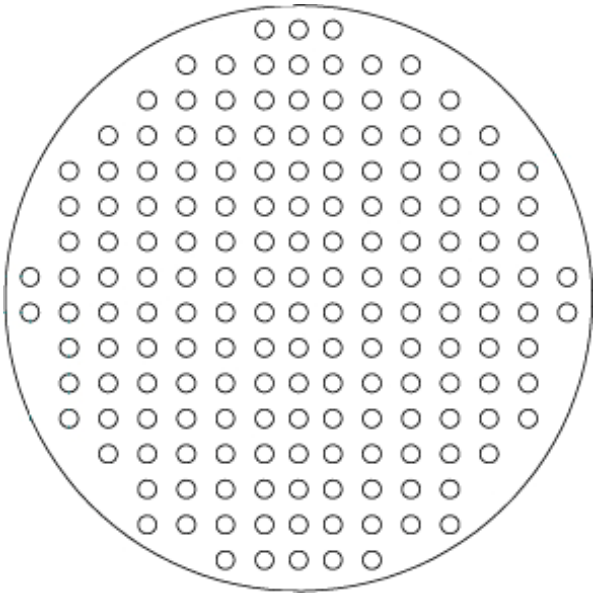

Figure 4.2 Inlet distributor of the riser (Li 2010)

Conservation equation of momentum for the solids phase

$$\frac{\partial}{\partial t}\left(\alpha_s \rho_s \vec{v}_s\right) + \nabla \cdot \left(\alpha_s \rho_s \vec{v}_s \vec{v}_s\right) = -\alpha_s \nabla p - \nabla p_s + \nabla \cdot \left(\overline{\overline{\tau_{s,m}}} + \overline{\overline{\tau_{s,t}}}\right) + \alpha_s \rho_s \vec{s} + K_{gs}\left(\vec{v}_g - \vec{v}_s\right) \quad (4)$$

where

$$\overline{\overline{\tau_{s,m}}} = \alpha_s \mu_{s,m}\left(\nabla \vec{v}_s + \nabla \vec{v}_s{}^T\right) - \frac{2}{3}\alpha_s \mu_{s,m} \nabla \cdot \vec{v}_s \,\overline{\overline{I}} + \lambda_s \nabla \cdot \vec{v}_s \,\overline{\overline{I}}$$

$$\overline{\overline{\tau_{s,t}}} = -\frac{2}{3}\alpha_s \rho_s k_s \overline{\overline{I}} + \alpha_s \mu_{s,t}\left(\nabla \vec{v}_s + \nabla \vec{v}_s{}^T\right) - \frac{2}{3}\alpha_s \mu_{s,t} \nabla \cdot \vec{v}_s \,\overline{\overline{I}}$$

K is the interphase exchange coefficient and $K_{gs}=K_{sg}$. Syamlal-O'Brien model (Syamlal and O'Brien 1986) is used in this study, where the value is based on measurements of terminal velocity $v_{s,\gamma}$:

$$K_{sg} = \frac{3\alpha_s\alpha_g\rho_g}{4v_{s,\gamma}^2 d_s}\left(0.63 + \frac{4.8}{\sqrt{Re_s/v_{s,\gamma}}}\right)^2 \left(\frac{Re_s}{v_{s,\gamma}}\right)\left|\vec{v}_s - \vec{v}_g\right| \quad (5)$$

$$v_{s,\gamma} = 0.5\left(A - 0.06Re_s + \sqrt{(0.06Re_s)^2 + 0.12Re_s(2B - A) + A^2}\right) \quad (6)$$

where $A=\alpha_g^{4.14}$, $B=0.8\alpha_g^{1.28}$ for $\alpha_g \leq 0.85$ and $B=a_g^{2.65}$ for $\alpha>0.85$ and $Re_s = \frac{\rho_g d_s\left|\vec{v}_s - \vec{v}_g\right|}{\mu_{g,m}}$

The solids pressure and viscosity are related to the granular temperature θ_s based on kinetic theory of granular flow. In the Syamlal-O'Brien model (Syamlal and O'Brien 2003), it is expressed by

$$p_s = 2\rho_s(1 + e_s)\alpha_s^2 g_{s,0}\Theta_s \quad (7)$$

where $g_{s,0}$ is radial distribution function $g_{s,0} = \left[1 - \left(\frac{\alpha_s}{\alpha_{s,max}}\right)^{\frac{1}{3}}\right]^{-1}$.

Solids shear viscosity

$$\mu_s = \mu_{s,m} = \mu_{s,col} + \mu_{s,kin} \quad (8)$$

Collisional viscosity

$$\mu_{s,col} = \frac{4}{5}{\alpha_s}^2 \rho_s d_s g_{s,0}(1+e_{ss})\left(\frac{\Theta_s}{\pi}\right)^{1/2} \tag{9}$$

Kinetic viscosity

$$\mu_{s,kin} = \frac{\alpha_s \rho_s d_s \sqrt{\Theta_s \pi}}{6(3-e_{ss})}\left[1+\frac{2}{5}g_{s,0}\alpha_s(1+e_{ss})(3e_{ss}-1)\right] \tag{10}$$

Bulk viscosity

$$\lambda_s = \frac{4}{3}\alpha_s \rho_s d_s g_{s,0}(1+e_{ss})\left(\frac{\Theta_s}{\pi}\right)^{1/2} \tag{11}$$

e_{ss} is the particle-particle restitution coefficient taken as empirical value 0.95 (Peng, Zhu, and Zhang 2010).

Granular temperature Θ_s is obtained by solving its transport equation:

$$\begin{aligned} &\frac{3}{2}\left[\frac{\partial}{\partial t}\left(\rho_s \alpha_s \Theta_s\right) + \nabla \cdot \left(\rho_s \alpha_s \vec{v}_s \Theta_s\right)\right] \\ &\qquad = \left[-p_s \bar{\bar{I}} + \left(\bar{\bar{\tau}}_s^m + \bar{\bar{\tau}}_s^t\right)\right] : \nabla \vec{v}_s + \nabla \cdot \left(k_{\Theta_s} \nabla \Theta_s\right) - \gamma_{\Theta_s} + \Phi_{gs} \end{aligned} \tag{12}$$

The diffusion coefficient of energy in Eq. (12) can be obtained by:

$$k_{\Theta_s} = \frac{15\alpha_s \rho_s d_s \sqrt{\Theta_s \pi}}{4(41-33\eta)}\left[1+\frac{12}{5}\eta^2(4\eta-3)\alpha_s g_{s,0} + \frac{16}{15\pi}(41-33\eta)\eta\alpha_s g_{s,0}\right] \tag{13}$$

where $\eta=1/2(1+e_{ss})$.

The collisionall dissipation of energy is calculated by:

$$\gamma_{\Theta_s} = \frac{12(1-e_s^2)g_{s,0}}{d_s\sqrt{\pi}}\rho_s{\alpha_s}^2{\Theta_s}^{3/2} \tag{14}$$

and the energy exchange between two phases is defined as $\phi_{gs}=-K_{gs}\theta_s$

(Gidaspow, Bezburuah, and Ding 1992).

k*-ε *turbulence model for the gas phase

$$\begin{aligned}\frac{\partial}{\partial t}\left(\alpha_g\rho_g k_g\right) + \nabla\cdot\left(\alpha_g\rho_g\,\vec{v}_g\,k_g\right) \\ = \nabla\cdot\left(\alpha_g\left(\mu_{g,m}+\frac{\mu_{g,t}}{\sigma_k}\right)\nabla k_g\right) + \left(\alpha_g G_{g,k} - \alpha_g\rho_g\varepsilon_g\right) + K_{sg}\left(C_{sg}\,k_s - C_{gs}\,k_g\right) \\ - K_{sg}\left(\vec{v}_s - \vec{v}_g\right)\frac{\mu_{s,t}}{\alpha_s\sigma_s}\nabla\alpha_s + K_{sg}\left(\vec{v}_s - \vec{v}_g\right)\frac{\mu_{g,t}}{\alpha_g\sigma_g}\nabla\alpha_g\end{aligned} \tag{15}$$

$$\begin{aligned}\frac{\partial}{\partial t}\left(\alpha_g\rho_g\varepsilon_g\right) + \nabla\cdot\left(\alpha_g\rho_g\,\vec{v}_g\,\varepsilon_g\right) \\ = \nabla\cdot\left(\alpha_g\frac{\mu_{g,t}}{\sigma_\alpha}\nabla\varepsilon_g\right) \\ + \frac{\varepsilon_g}{k_g}\Bigg\{C_{1\varepsilon}\alpha_g G_{g,k} - C_{2\varepsilon}\alpha_g\rho_g\varepsilon_g \\ + C_{3\varepsilon}\Bigg[K_{sg}\left(C_{sg}\,k_s - C_{gs}\,k_g\right) - K_{sg}\left(\vec{v}_s - \vec{v}_g\right)\frac{\mu_{s,t}}{\alpha_s\sigma_s}\nabla\alpha_s \\ + K_{sg}\left(\vec{v}_s - \vec{v}_g\right)\frac{\mu_{g,t}}{\alpha_g\sigma_g}\nabla\alpha_g\Bigg]\Bigg\}\end{aligned} \tag{16}$$

where $\mu_{g,t} = \rho_g C_\mu \frac{k_g^2}{\varepsilon_g}$ and $C_\mu = 0.09$.

k*-ε *turbulence model for the solids phase:

$$\begin{aligned}\frac{\partial}{\partial t}(\alpha_s \rho_s k_s) + \nabla \cdot (\alpha_s \rho_s \vec{v}_s k_s) \\ = \nabla \cdot \left(\alpha_s \left(\mu_{s,m} + \frac{\mu_{s,t}}{\sigma_k}\right) \nabla k_s\right) + (\alpha_s G_{s,k} - \alpha_s \rho_s \varepsilon_s) + K_{gs}(C_{gs} k_g - C_{sg} k_s) \\ - K_{gs}(\vec{v}_g - \vec{v}_s) \frac{\mu_{g,t}}{\alpha_g \sigma_g} \nabla \alpha_g + K_{gs}(\vec{v}_g - \vec{v}_s) \frac{\mu_{s,t}}{\alpha_s \sigma_s} \nabla \alpha_s\end{aligned} \tag{17}$$

$$\begin{aligned}\frac{\partial}{\partial t}(\alpha_s \rho_s \varepsilon_s) + \nabla \cdot (\alpha_s \rho_s \vec{v}_s \varepsilon_s) \\ = \nabla \cdot \left(\alpha_s \frac{\mu_{s,t}}{\sigma_\alpha} \nabla \varepsilon_s\right) \\ + \frac{\varepsilon_s}{k_s} \Big\{ C_{1\varepsilon} \alpha_s G_{s,k} - C_{2\varepsilon} \alpha_s \rho_s \varepsilon_s \\ + C_{3\varepsilon} \Big[K_{gs}(C_{gs} k_g - C_{sg} k_s) - K_{gs}(\vec{v}_g - \vec{v}_s) \frac{\mu_{g,t}}{\alpha_g \sigma_g} \nabla \alpha_g \\ + K_{gs}(\vec{v}_g - \vec{v}_s) \frac{\mu_{s,t}}{\alpha_s \sigma_s} \nabla \alpha_s \Big] \Big\}\end{aligned} \tag{18}$$

where $\mu_{s,t} = \rho_s C_\mu \frac{k_s^2}{\varepsilon_s}$ and $C_\mu = 0.09$.

Catalytic ozone decomposition

The catalytic ozone decomposition reaction is a simple irreversible first-order reaction expressed as $O_3 \xrightarrow{\text{catalyst}} 1.5O_2$. The species transport equations are used to solve the mass fraction of each species in the mixture of the gas phase.

Ozone

$$\frac{\partial}{\partial t}\left(\alpha_g \rho_{O_3} Y_{O_3}\right) + \nabla \cdot \left(\alpha_g \rho_{O_3} \vec{v}_g Y_{O_3}\right) = -\nabla \cdot \alpha_g \bar{J}_{O_3} + R_{O_3} \quad (19)$$

where $\bar{J}_{O_3} = -(\rho_{O_3} D_{O_3} + \frac{\mu_{g,t}}{Sc_t})\nabla Y_{O_3}$, D is the mass diffusion coefficient and Sc_t is the turbulent Schmidt number.

Oxygen

$$\frac{\partial}{\partial t}\left(\alpha_g \rho_{O_2} Y_{O_2}\right) + \nabla \cdot \left(\alpha_g \rho_{O_2} \vec{v}_g Y_{O_2}\right) = -\nabla \cdot \alpha_g \bar{J}_{O_2} + R_{O_2} \quad (20)$$

where $\bar{J}_{O_2} = (\rho_{O_2} D_{O_2} + \frac{\mu_{g,t}}{Sc_t})\nabla Y_{O_2}$.

R is the first-order reaction rate based on the catalyst particle volume fraction. For ozone, it can be written as:

$$R_{O_3} = -\frac{\partial C_{O_3}}{\partial t} = W A_p k_r C_{O_3} \quad (21)$$

k_r is the reaction rate constant , which is determined by experimental data. It can also be also expressed by Arrhenius equation $k_r = z e^{-E_a/rT}$. z, E_a, r and T are the pre-

exponential factor, activation energy, universal gas constant and temperature respectively. According to the experiments, k_r =4x10^{-5}m/s (Li 2010). A_p is particle surface area per unit volume. Assuming the shape of particles is sphere, so

$$A_p = \frac{\alpha_s}{\frac{1}{6}\pi d_s^3} \cdot \pi d_s^2 = \frac{6\alpha_s}{d_s} \tag{22}$$

and W is an empirical coefficient valued 0 to 1 to correct the numerical reaction rate.

4.3.2 Computational domain and boundary conditions

Two-dimensional simulations of the CFB riser shown in Figure 4.1 are carried out in this study. The computational domain is of 10m × 0.0381m according to the dimensions of the CFB riser. The schematic diagram of the computational domain and boundary conditions are shown in Figure 4.3. The boundary conditions at the inlet, outlet and wall are set up according to actual conditions in the riser.

Inlet: the profiles of the velocities of gas and solids, and volume fraction of solids are specified according to the inlet distributor used in the experiment as well as the flow rates of both gas and solid phases. There are 6.5 jets set up along the radius illustrated on Figure 4.4.

Outlet: the relative pressure at the outlet of the riser is specified as zero.

Wall: for the gas phase, no slip velocity on the wall is used. For the solids phase, the particles can slip on the wall based on the Jackson and Johnson theory (Johnson and Jackson 1987). The shear stress and collision energy are:

$$\tau_s = -\frac{\sqrt{3}\pi\rho_s g_{s,0}\alpha_s\phi\sqrt{\Theta_s}}{6\alpha_{s,max}} \tag{23}$$

$$q_s = \frac{\pi}{6}\sqrt{3}\phi\frac{\alpha_s}{\alpha_{s,max}}\rho_s g_{s,0}\sqrt{\theta_s}\upsilon_{s,w}^2 - \frac{\pi}{4}\sqrt{3}\frac{\alpha_s}{\alpha_{s,max}}\left(1-e_{s,w}^2\right)\rho_s g_{s,0}\theta_s^{\frac{3}{2}} \tag{24}$$

In Eqs. (23) and (24), ϕ is the specularity coefficient and $e_{s,w}$ is the particle-wall restitution coefficient. The second term in Eq. (24) represents the energy loss by collision between particle and wall. . The specularity coefficient describes the roughness of the wall to determine the momentum transfer due to the collision between the particle and wall with the value between 0 for perfectly specular collision and 1 for perfectly diffuse collision. Particle-wall restitution coefficient is the parameter determining the dissipation energy per particle-wall collision. Both of the specularity coefficient and restitution coefficient are empirical to determined by the experiments results (Benyahiaa, Syamlala, and O'Brien 2005; Almuttahar and Taghipour 2008; Wang et al. 2010; Li, Grace, and Bi 2010; Lan et al. 2012).

4.3.3 Solver

The double-precision segregated, implicit formulations and unsteady solver are selected. The phase-coupled SIMPLE algorithm is applied for the pressure-based solver. The discretization scheme for all convection terms is the second-order upwind scheme

except for the volume fraction equation where the QUICK scheme is used. A convergence criterion of 10^{-4} for each scaled residual component is specified except for the species fraction, where 10^{-5} is used. The commercial CFD software ANSYS FLUENT 13.0 is used to carry out the simulations with parallel 2.4Ghz nodes. The operating conditions and parameters in the numerical simulations are presented in Table 4.1.

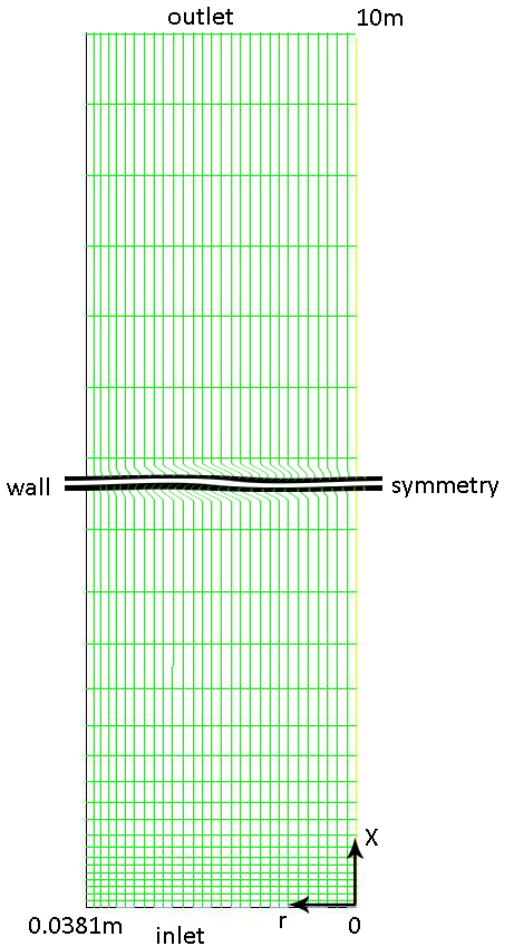

Figure 4.3 Computational domain, mesh and boundary conditions

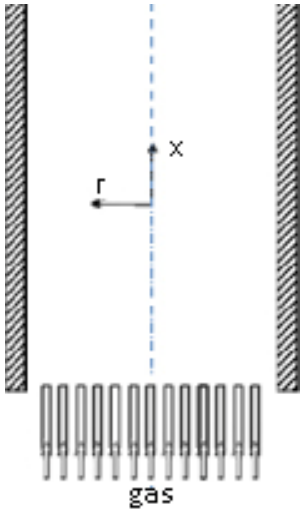

Figure 4.4 Schematic diagram of gas velocity at the inlet of the riser

Table 4.1 Operating conditions and parameters for the simulations

Gas density ($\mathrm{kg/m^3}$)	1.225
Gas viscosity ($\mathrm{kg/(m \cdot s)}$)	1.7894×10^{-5}
Particle density ($\mathrm{kg/m^3}$)	1730
Particle diameter ($\mu\mathrm{m}$)	60, 120, 240
Superficial gas velocity ($\mathrm{m/s}$)	3, 5, 8.3
Particle circulation rate ($\mathrm{kg/(m^2 \cdot s)}$)	50, 100, 200
Particle-particle restitution coefficient	0.95
Particle-wall restitution coefficient	0.9
Specularity coefficient	0.0001

4.4 Results and discussion

First, to verify whether the solutions reach “steady-state” from the unsteady simulation, the dimensionless ozone concentration at x=5m of the CFB riser is monitored during the simulation. Figure 4.5 shows that the time-average dimensionless ozone concentration at the radial position of r/R= 0.5 and the axial position of x= 5m. It is clear that the dimensionless ozone concentration at that point is nearly unchanged, with oscillation less in 1%, after 5 sec of flow time. Thus, the solutions are considered as steady time-

averaged solutions. All the results presented in this study are the steady-state solutions to guarantee the solutions independent of the time.

4.4.1 Grid independence study

Figure 4.6 shows the results of the grid independence study. It clearly shows that the results using the grids of 12,093, 23,577 and 46,690 cells are almost identical, thus the grid of 12,093 is used in this study.

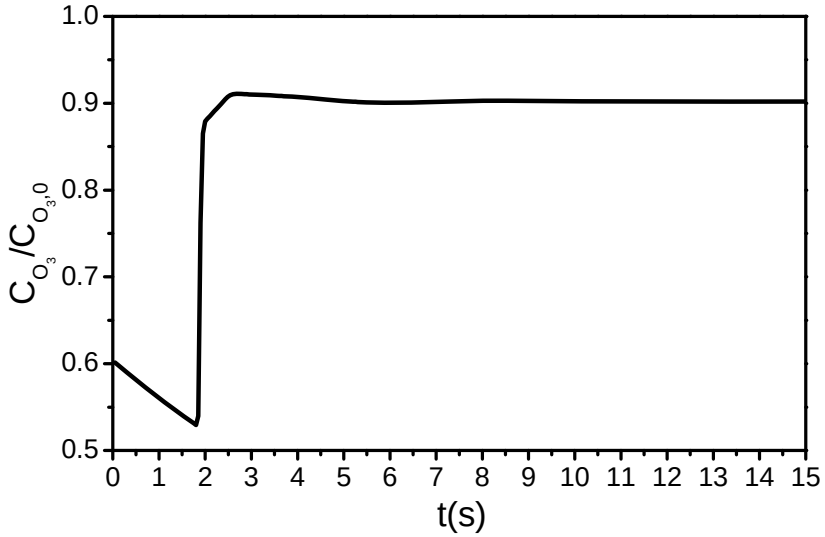

Figure 4.5 Time-average dimensionless ozone concentration at r/R=0.5 and x=5m

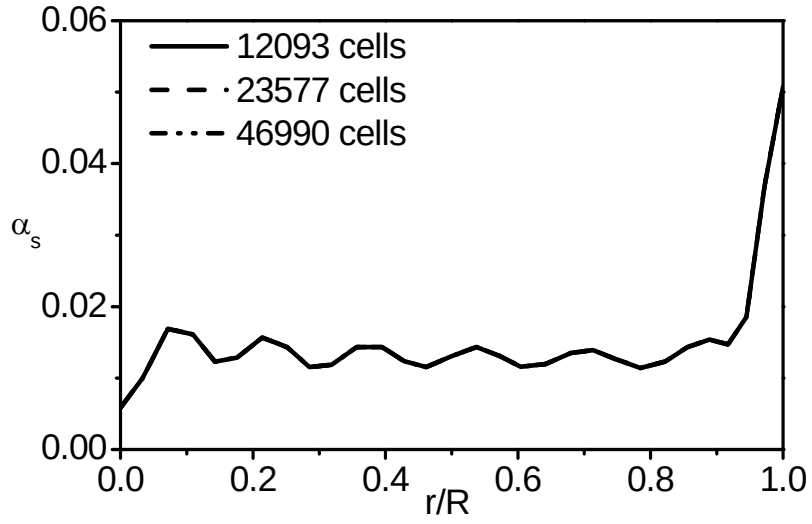

Figure 4.6 Radial profile of the solids volume fraction at 4.78m with different meshes

4.4.2 Time independence study

The Figure 4.7 shows the results of numerical simulations using time steps 0.0001s and 0.00001s. From Figure 3.7, it can be seen that the results of the time step 0.0001s and 0.00001s are almost the same, thus the time step 0.0001s is used in this study.

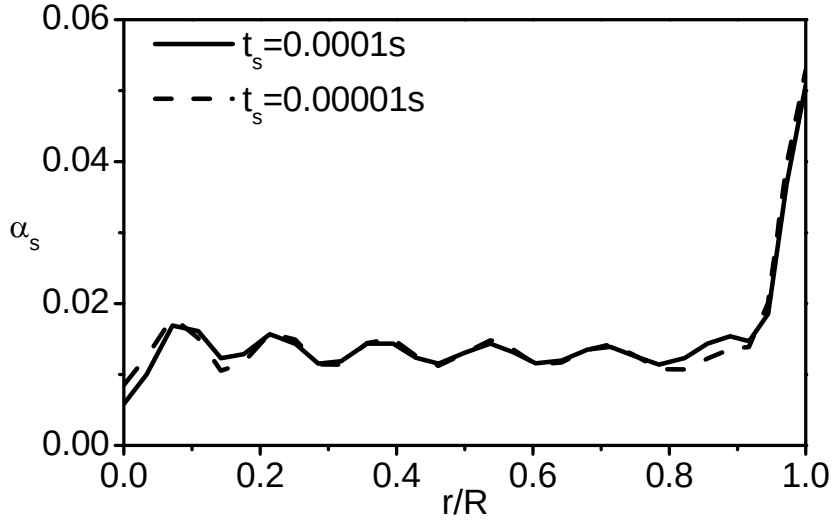

Figure 4.7 Radial profile of the solids volume fraction at 4.78m with different time steps

4.4.3 Ozone concentration

Ozone concentration in the CFB riser depends on the rate of reaction catalyzed by the solid particles. The lower ozone concentration means more ozone is decomposed to oxygen. As the reaction catalyzed by solid particles, the ozone concentration strongly depends on the solids volume fraction. The solid particles are dilute in the centre and dense near the wall in the CFB riser due to the core-annulus solids distribution in the radial direction. Thus, the ozone concentration should be lower near the wall than that in the centre. The reaction rate can be calculated by Eq. (21). Since the reaction is defined as a one-step reaction, it is assumed in the numerical simulations that the ozone is catalyzed once it contacts with solid particles. However, in reality, there are multiple-step reactions during this catalysing process from the surface to the core of the particles. Therefore, the coefficient W is used in Eq. (21) as a correction factor to account for the effect of multiple-step reactions. Simulations are carried out using W=0.5 and W=1.0 and the distributions of the normalized ozone concentration in the radial direction at different axial locations in the riser under the different operating conditions are given in Figure 4.8. C_{O_3} is the ozone concentration in the riser and $C_{O_3,0}$ is the ozone concentration at the inlet, which is 20ppm. It can be seen from Figure 4.8 that the ozone concentration is low near the wall from both experiments and simulations. At x=0.11m, which is very close to the inlet, the ozone is barely decomposed, where the normalized concentration is close to 1. Along the axial direction in the riser, the ozone begins to decompose into oxygen, so the ozone concentration decreases from the inlet to the outlet of the riser. And above 2.39m from the inlet, the rate of ozone decomposition is

slow down because the solids volume fraction alone the riser, especially near the wall, is also decreased. Apparently, W=0.5 results in higher ozone concentration than W=1 since the reaction rate is lower when W is lower. It is also found that W=0.5 gives better agreement with the experimental data. The overall agreement between the numerical results and experimental data using W=0.5 is good. However, the agreement is better at higher superficial gas velocity than that at lower superficial gas velocity. Larger discrepancy between the numerical simulations and experiments occurs near the riser outlet when the superficial gas velocity is low. The discrepancy might be caused by the fact that the riser inlet is not axisymmetric, so the flow in the riser is three-dimensional. However, the simulations are carried out as two-dimensional due to the prohibitive cost of the three-dimensional simulation in the CFB riser. Also, the mesh size and the time step could contribute to this discrepancy which is discussed in Appendix.

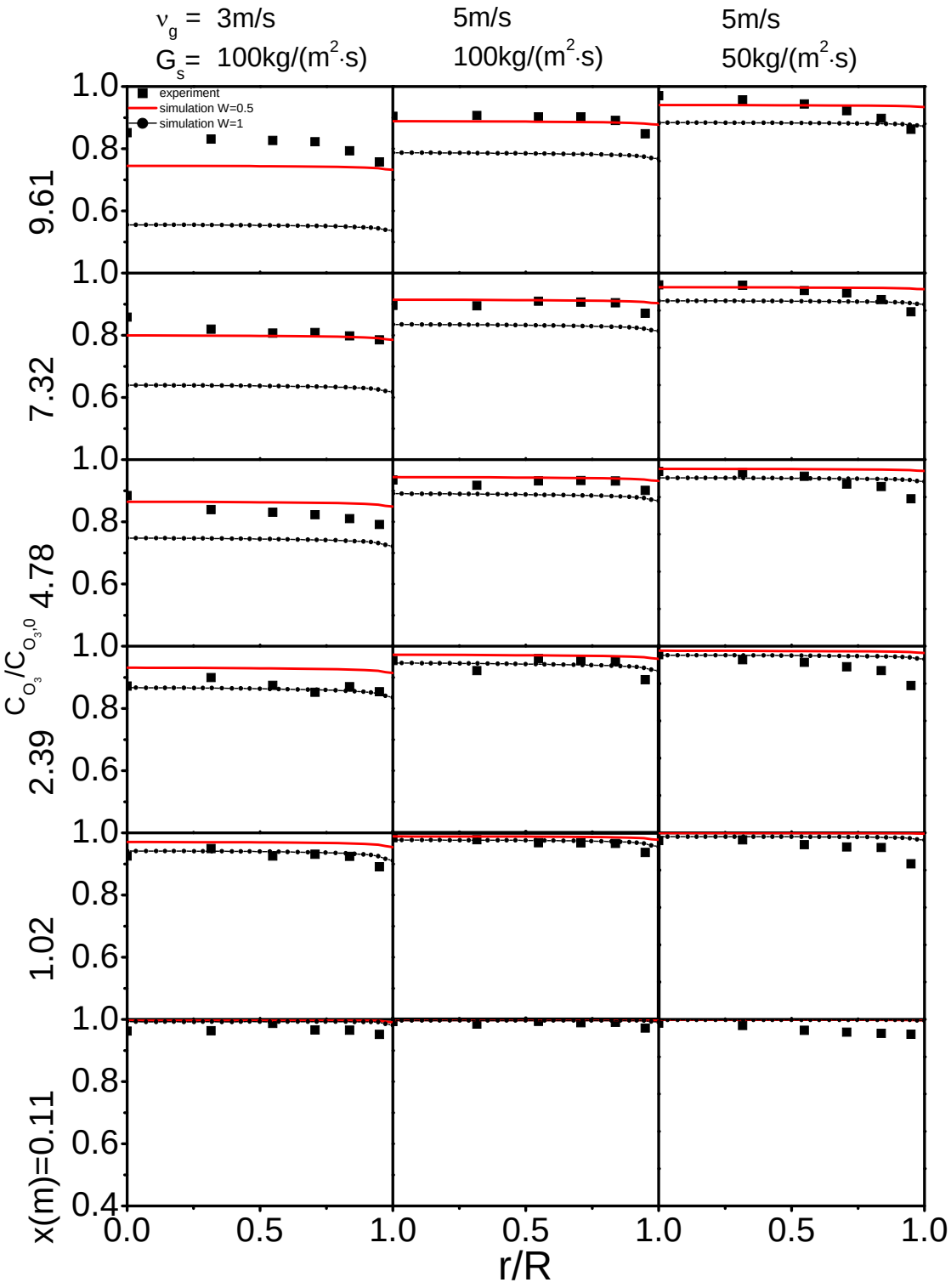

Figure 4.8 Normalized ozone concentration along the radial direction at different axial locations under three operating conditions (simulation vs. experiments data)

Comparing the results from different operating conditions, it is found that the operating conditions with lower superficial gas velocity and higher particle circulation rate, i.e. the case with v_g=3 m/s and G_s=100 kg/(m^2·s), result in lower ozone concentration (i.e. a higher ozone decomposition conversion) as shown in Figure 4.8. Near the outlet of the riser (at x=9.61m), the normalized ozone concentration is around 0.73. This is due to higher solids volume fraction in the riser, which results from lower superficial gas velocity and higher particle circulation rate under this operating condition, which leads to more reactions. And the operating conditions with higher superficial gas velocity and lower particle circulation rate, i.e. the case with v_g=5 m/s and G_s=50 kg/(m^2·s), result in very low solids volume fraction in the riser, and therefore higher normalized ozone concentration at outlet of the riser (x=9.61m), which is about 0.95. So, only 5% of ozone is decomposed into oxygen. The ozone concentration at the outlet of the riser for the case with higher superficial gas velocity and higher particle circulation rate, i.e. the case with v_g=5 m/s and G_s=100 kg/(m^2·s), is about 0.90. This trend occurs in both the experiments and simulations. To fully understand the trend under different operating conditions, simulations under the operating conditions of v_g=8.3 m/s, G_s=100 kg/(m^2·s) and v_g=5 m/s, G_s=200 kg/(m^2·s) are also conducted as supplements. The normalized ozone concentrations are given in Figure 4.9. It is clear that the ozone concentration decreases with the decrease in the superficial gas velocity or the increase in the solids circulation rate. Table 4.2 provides the ozone conversion rate in the riser under different operating conditions. The variation of the ozone conversion rate is quite quasi-linear in term of the superficial gas velocity or solids circulation rate.

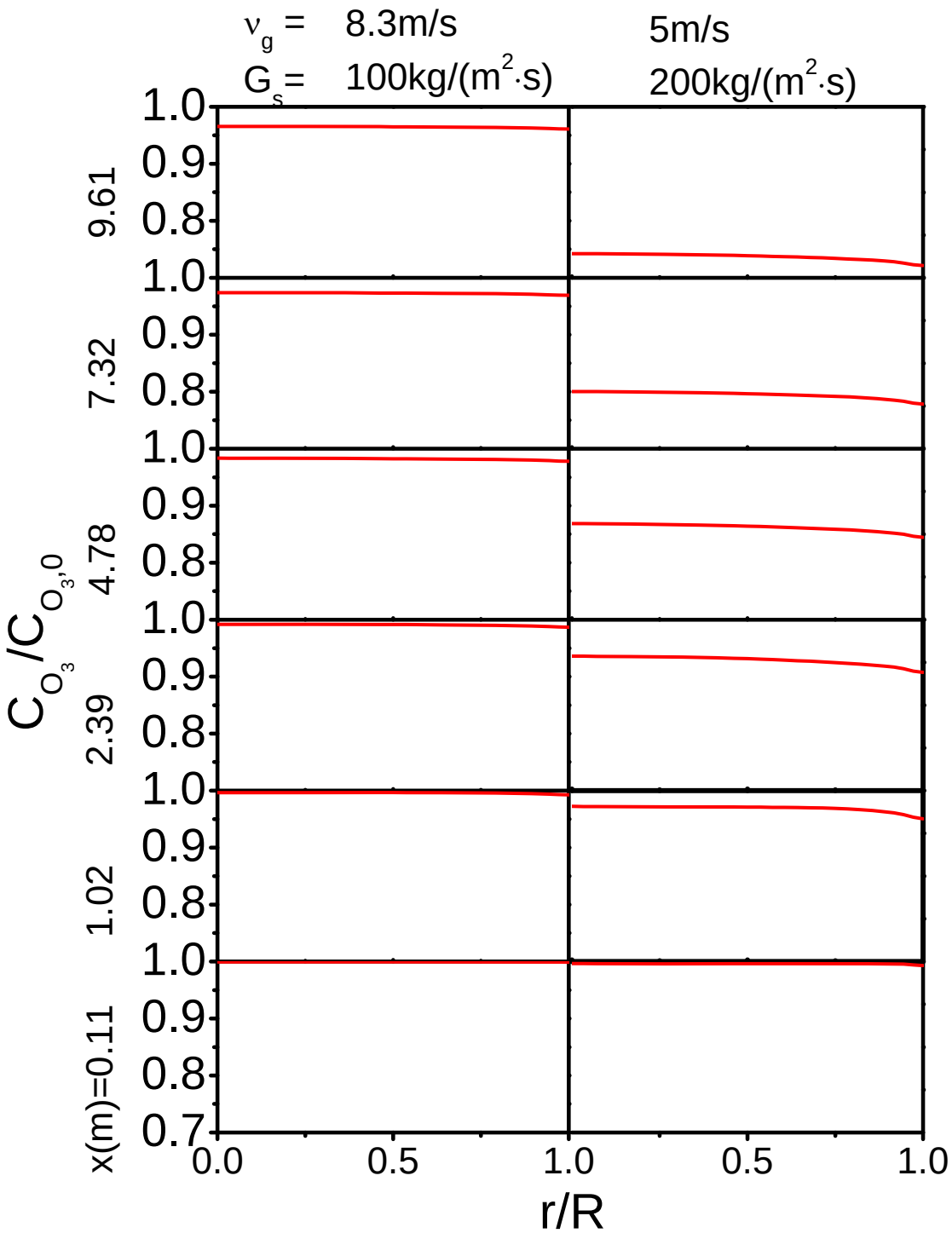

Figure 4.9 Normalized ozone concentration along the radial direction at different axial locations for v_g=8.3 m/s G_s=100 kg/(m^2·s) and =5 m/s G_s=200 kg/(m^2·s)

Table 4.2 Ozone conversion rate in the riser under different operating conditions

Conversion of ozone G_s / v_g	50 kg/(m^2·s)	100 kg/(m^2·s)	200 kg/(m^2·s)
3 m/s		26.6%	
5 m/s	5.28%	9.86%	18.2%
8.3 m/s		3.68%	

The effect of particle size on the ozone conversion is also investigated with the particle diameters of 60μm, 120μm and 240μm. According to Eq. (21), when k_r and W are constants, the reaction rate equation is only with respect to A_p, the particle surface area per unit volume. Assuming that the particles are spherical, as defined in Eq. (22), the reaction rate is charged by the fraction α_s/d_s, which is the solids volume fraction over the particle diameter. When the particle diameter increases, the contact surface per particle mass between gas and particles will decrease, so, the reaction rate will be lower. However, the mass of the particle will increase if the particle diameter increases when the solids density is constant. This leads to a lower particle velocity, which in turn results in a higher solids volume fraction. And higher solids volume fraction also contributes to the increase of the reaction rate. Thus, when the particle diameter increases, there are two opposite effects on the reaction rate. The simulation results of normalized ozone concentration with different particle sizes are illustrated in Figure 4.10. It is clear that the particle size has a great effect on the ozone concentration and larger particle size leads to higher ozone concentration, which represents lower ozone conversion (i.e. lower reaction rate). Therefore, with different particle sizes, the contact surface area between gas and particles is playing in a major role in the reaction rate.

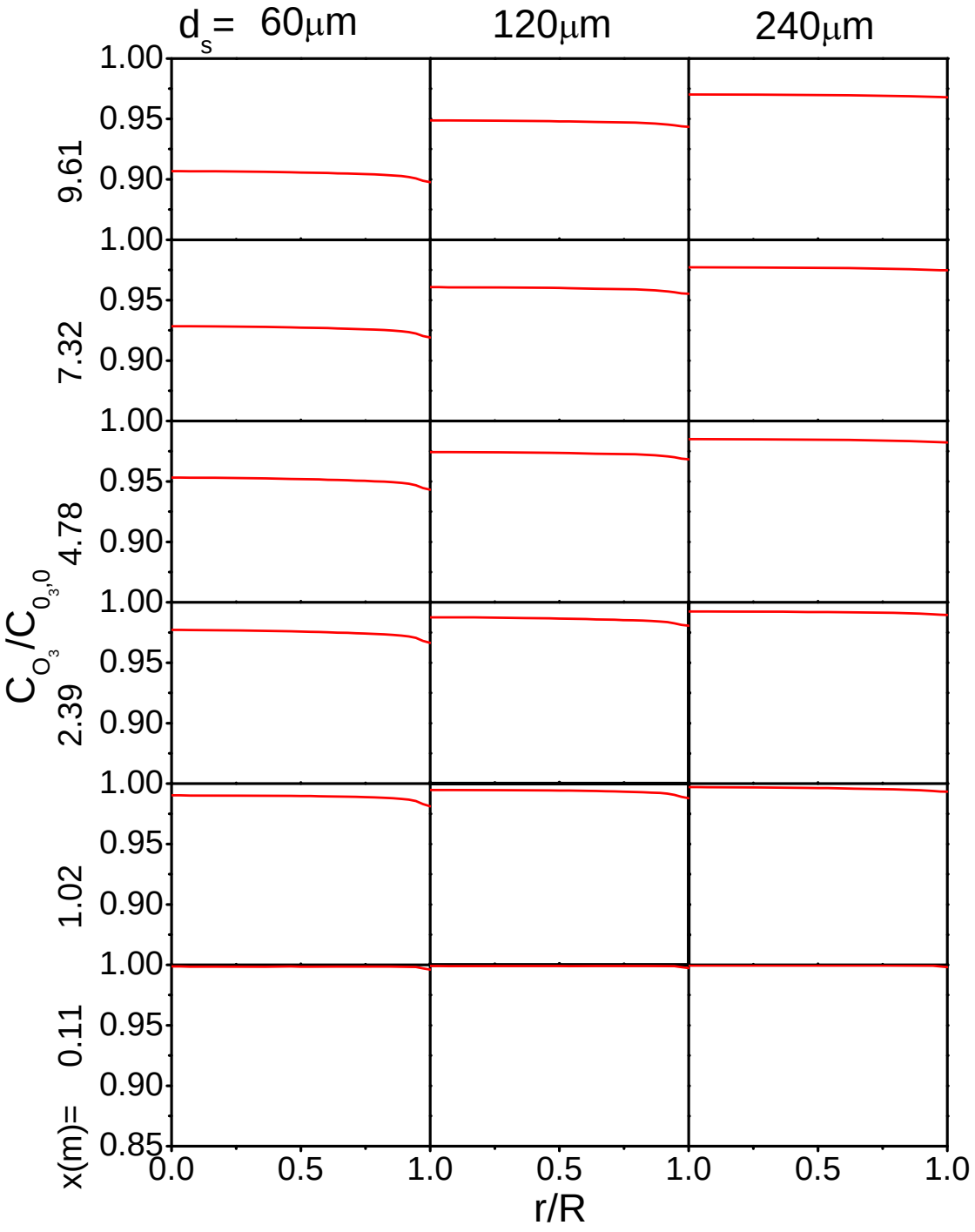

Figure 4.10 Normalized ozone concentration along the radial direction at different axial locations with different particle diameters

4.5 Conclusions

The CFD model for the catalytic ozone decomposition in a gas-solids circulating fluidized bed riser is presented based on the Eulerian-Elerian method with the kinetic theory of granular flow. The catalytic ozone decomposition reaction is defined as a first-order reaction with a one-step reaction rate equation. An empirical coefficient (W) in the reaction rate equation is introduced and W =0.5 is proposed. The 2D simulations are carried out under different operating conditions and the results are compared with the experimental data to validate generality of the proposed comprehensive CFD model. The results show that the ozone concentration strongly depends on the core-annulus solid distribution. The ozone concentration decreases with the decrease in the superficial gas velocity or the increase in the solid circulation rate. And the particle size plays a major role on the reaction contributed by the contact surface area between two phases. However, there is still need in the future study on 3D simulations and more complex reaction models.

Nomenclature

A_p = particle surface area per unit volume, m
C_{O3} = ozone concentration, ppm
C_μ = turbulence constant, dimensionless
$C_{1\varepsilon}$ = turbulence constant, dimensionless
$C_{2\varepsilon}$ = turbulence constant, dimensionless
$C_{3\varepsilon}$ = turbulence constant, dimensionless
D = mess diffusion coefficient, dimensionless
d = diameter, m
e= restitution coefficient, dimensionless
G_s = solids circulation rate, $kg/m^2 \cdot s^{-1}$
g = gravity, m/s^2
$g_{s,0}$ = radial distribution function, dimensionless
I = unit matrix, dimensionless
K = interphase exchange coefficient, $kg/m^3 \cdot s^{-1}$
k = turbulence kinetic energy, m^2/s^2
k_r = reaction rate constant, s^{-1}
$k_{\theta s}$= diffusion coefficient of energy, $kg/m \cdot s^{-1}$
p = pressure, Pa
q = collision energy, kg/s^{-3}
R= radius of the riser, m
r = radial coordinate, m
Re = Reynolds number, dimensionless
Sc_t = turbulent Schmidt number, dimensionless
t= time, s
v = velocity, m/s
x = axial coordinate, m
Y = species concentration, dimensionless

Greek symbols

α = volume fraction, dimensionless
γ = collision dissipation of energy, $kg/m \cdot s^{-3}$
ε = turbulence dissipation rate, m^2/s^3
θ = granular temperature, m^2/s^2
λ = bulk viscosity, $kg/m \cdot s^{-1}$
μ = viscosity, $kg/m \cdot s^{-1}$
ρ = density, kg/m^3
τ = stress tensor, Pa
Φ = energy exchange coefficient, $kg/m \cdot s^{-3}$
ϕ = specularity coefficient, dimensionless

Subscripts

g = gas phase
s = solids phase
m= molecular
t = turbulence
w= wall

References

Almuttahar, A., & Taghipour, F. (2008). Computational fluid dynamics of high density circulating fluidized bed riser: Study of modeling parameters. *Powder Technology , 185*, pp. 11-23.

Benyahiaa, S., Syamlala, M., & O'Brien, T. J. (2005). Evaluation of boundary conditions used to model dilute, turbulent gas/solids flows in a pipe. *Powder Technology , 156*, pp. 62 – 72.

Bi, H., Jiang, P., Jean, R. -H., & Fan, L. -S. (1992). Coarse-particle effects in a multisolid circulating fluidized bed for catalytic reactions. *Chemical Engineering Science , 47* (12), pp. 3113-3124.

Bolland, O., & Nicolai, R. (2001). Describing mass transfer in circulating fluidized beds by ozone decomposition. *Chemical Engineering Communications , 187* (1), pp. 1-21.

Cheng, Y., Guo, Y., Wei, F., & Jin, Y. (2001). CFD simulation of 221s in the entrance region of a downer. *Chem. Eng. Sci. , 56* (4), pp. 1687–1696.

Cheng, Y., Guo, Y., Wei, F., Jin, Y., & Lin, W. (1999). Modeling the hydrodynamics of downer reactors based on kinetic theory. *Chem. Eng. Sci. , 54* (13-14), pp. 2019-2927.

Cruz, E., Steward, F. R., & Pugsley, T. (2006). New closure models for CFD modeling of high-density circulating fluidized beds. *Powder Technology , 169*, pp. 115–122.

Dasgupta, S., Jackson, R., & Sundaresan, S. (1994). Turbulent gas-particle flow in vertical risers. *AICHE Journal , 40* (2), pp. 215-228.

Ding, J., & Gidaspow, D. (1990). A bubbling fluidization model using kinetic theory of granular flow. *AIChE Journal , 36* (4), pp. 523–538.

Dong, W. G., Wang, W., & Li, J. H. (2008). A multiscale mass transfer model for gas–solid riser flows: part II—sub-grid simulation of ozone decomposition. *Chemical Engineering Science , 63*, pp. 2811 – 2823.

Gidaspow, D., Bezburuah, R., & Ding, J. (1992). Hydrodynamics of circulating fluidized beds, kinetic theory approach. In *Fluidization VII: Proceedings of the 7th Engineering Foundation Conference on Fluidization.* 75-82.

Grace, J. R. (1990). High-velocity fluidized bed reactors. *Chemical Engineering Science , 45* (8), pp. 1953–1966.

Grace, J. R., & Bi, H. (1997). Introduction to circulating fluidized beds. In J. R. Grace, A. Avidan, & T. Knowlton, *Circulating fluidized beds* (pp. 1-19). New York: Engineering Foundation.

Hansen, K. G., Solberg, T., & Hjertager, B. H. (2004). A three-dimensional simulation of gas/particle flowand ozone decomposition in the riser of a circulating fluidized bed. *Chemical Engineering Science , 59*, pp. 5217 – 5224.

Helland, E., Bournot, H., Occelli, R., & Tadrist, L. (2007). Drag reduction and cluster formation in a circulating fluidised bed. *Chemical Engineering Science , 62* (1-2), pp. 148-158.

Hrenya, C. M., & Sinclair, J. L. (1997). Effects of particle-phase turbulence in gas-solid flows. *AIChE Journal , 43* (4), pp. 853-869.

Huang, W., Yan, A., & Zhu, J. (2007). Hydrodynamics and flow development in a 15.1 m circulating fluidized bed riser. *Chem. Eng. & Technol , 30* (4), pp. 460-466.

Huang, W., Zhu, J., & Parssinen, J. H. (2006). Comprehensive study on solids acceleration length in a long CFB riser. *29* (10), 1197-1204.

Jiang, P., Bi, H., Jean, R. H., & Fan, L. S. (1991). Baffle effects on performance of catalytic circulating fluidized bed reactor. *AIChE Journal , 37* (9), 1392-1400.

Jiang, P., Inokuchi, K., Jean, R. H., Bi, H., & Fan, L. S. (1990). Ozone decomposition in a catalytic circulating fluidized bed reactor. In P. Basu, M. Horio, & M. Hasatani, *Circulating Fluidized Bed Technology III* (pp. 557-562). Oxford: Pergamon Press.

Johnson, P. C., & Jackson, R. (1987). Frictional-collisional constitutive relations for granular materials, with application to plane shearing. *J. Fluid Mech. , 176*, pp. 67-93.

Kagawa, H., Mineo, H., Yamazaki, R., & Yoshida, K. (1990). A gas-solid contacting model for fast fluidized bed. In P. Basu, M. Horio, & M. Hasatani, *Circulating Fluidized Bed Technology III* (pp. 551-556). Oxford: Pergamon Press.

Lan, X. Y., Xu, C. M., Gao, J. S., & Al-Dahhan, M. (2012). Influence of solid-phase wall boundary condition on CFD simulation of spouted beds. *Chemical Engineering Science , 69*, pp. 419-430.

Li, D. B. (2010). *Investigation of circulating fluizied bed riser and downer reactor performance for catalytic ozone decompostion.* Phd Thesis, Univ. of Western Onatario.

Li, T. W., Grace, J., & Bi, X. T. (2010). Study of wall boundary condition in numerical simulations of bubbling fluidized beds. *Powder Technology , 203*, pp. 447-457.

Miller, A., & Gidaspow, D. (1992). Dense, vertical gas–solids flow in a pipe. *AIChE J. , 38*, pp. 1801-1813.

Ouyang, S., Li, X. G., & Potter, O. E. (1995). Circulating fluidized bed as a catalytic reactor: experimental study. *AIChE Journal , 41* (6), pp. 1534–1542.

Ouyang, S., Lin, J., & Potter, O. E. (1993). Ozone decomposition in a 0.254 m diameter circulating fluidized bed reactor. *Powder Technology , 74* (1), pp. 73-78.

Peng, B. T., Zhu, J., & Zhang, C. (2010). Numerical study on the effect of the air jets at the inlet distributor in the gas-solids circulating fluidized-bed risers. *Ind. Eng. Chem. Res. , 49*, pp. 5310–5322.

Qi, X., Huang, W., Pan, Y., Zhu, J., & Shi, Y. (2003). Investigation on solids concentration and core-annulus flow structure in circulating fluidized bed risers. *J. Sichuan Univ. , 35* (1), pp. 43-47.

Reh, L. (1999). Challenges of circulating fluid-bed reactors in energy and raw materials industries. *Chemical Engineering Science , 54* (22), pp. 5359–5368.

Syamlal, M., & O'Brien, T. (1986). Computer simulation of bubbles in a fluidized bed. *AIChE Symposium Series , 85*, pp. 22-31.

Syamlal, M., & O'Brien, T. (2003). Fluid dynamic simulation of O3 decomposition in a bubbling fluidized bed. *AIChE Journal , 49* (11), pp. 2793–2801.

Therdthianwong, A., Pantaraks, P., & Therdthianwong, S. (2003). Modeling and simulation of circulating fluidized bed reactor with catalytic ozone decomposition reaction. *Powder Technology , 133*, pp. 1– 14.

Wang, X. F., Jin, B. S., Zhong, W. Q., & Xiao, R. (2010). Modeling on the hydrodynamics of a high-flux circulating fluidized bed with geldart group a particles by kinetic theory of granular flow. *Energy Fuels , 24*, pp. 1242–1259.

Yan, A., & Zhu, J. (2004). Scale-up effect of riser reactors (1) axial and radial solids concentration distribution and flow development. *Ind & Eng Chem Res , 43* (19), pp. 5810-5819.

Zhu, J. X., & Cheng, Y. (2005). Fluidized-Bed Reactors and Applications. In C. Crowe (Ed.), *Multiphase Flow Handbook* (pp. 5.55-5.93). New York: CRC Press.

Chapter 5.

5 Conclusions and recommendations

5.1 Conclusions

Ozone decomposition as a model reaction for the study of the characteristics of the gas-solids reactions in CFB reactors depends strongly on the aerodynamics of the two-phase flow. Studies on aerodynamics and reactions are important to improve the circulating fluidized bed (CFB) designs. For this purpose, a CFD model for the simulations of the gas-solids two-phase flows with reactions in a CFB riser has been developed and validated in this study. The Eulerian-Eulerian method with the kinetic theory of granular is adopted to describe the flow of the solids phase. A turbulence model is applied in both gas and solids phases. The effect of the specularity coefficient and particle-wall restitution coefficient in the Jackson and Johnson wall boundary condition on the solids phase flows has been investigated in order to correctly predict the solid particle distribution near the wall. The numerical results under different operating conditions are compared with the experimental data for the solids volume fraction, solids velocity and ozone concentrations in the radial and axial directions to validate the generality of the proposed CFD model. And the effect of the particle size on the reactions has also been investigated.

It has been found that the specularity coefficient has a strong effect on the solid particle distribution near the wall and the effect becomes weaker with the increase in the particle-wall restitution coefficient; the particle-wall restitution coefficient has a less

effect on the solid particle distribution near the wall than that of specularity coefficient and the effect is less when the specularity coefficient decreases. Moreover, the wall affects the solid particle lateral velocity and changes the solids distribution near the wall. The higher the lateral velocity of particle, the lower the solids volume fraction near the wall is. The proposed CFD model has been tested under different operating conditions and the numerical results are compared with the experiment data for the radial and axial distributions. The agreement with the experiments for the solids volume fraction and velocity is good in the upper region of the riser. The difference between the numerical and experimental results is relatively large at the bottom of the CFB riser.

In this study, a one-step reaction is used to define the ozone decomposition. However, in reality, the reaction occurs on the surface and inside of the particles, resulting in a lower reaction rate than that of the one-step assumption. Thus, an empirical correction factor is introduced and it is approved in this study that this correction factor should be 0.5 by comparing the predicted ozone concentration distributions in both radial and axial directions with the experimental results. In addition, it is demonstrated that the particle size has great effects on the reaction rate. A larger particle diameter will result in a lower reaction rate (i.e. lower ozone conversion).

5.2 Recommendations

There are still some issues that have not been dealt with in this study, and further works need to be done in term of the following:

(1) The particle size is a significant factor affecting the aerodynamics in the fluidized

beds. In experiments, the particles size is measured as an average value after weeks removing fines process. Actually, the stable particle size distribution is set up as a constant for only one solids phase in the simulation, where the experimental stable particle size distribution is similar to Gaussian distribution reported by Li (2010). So multiple particles sizes could be considered to describe the actual particle phase.

(2) In this study, the flow at the inlet is not axisymmetric according to the experiment, and the best treatment for this case thus is the 3D simulation.

(3) In term of the ozone concentration, in the Eulerian-Eulerian multiple phase approach, a one-step reaction is applied ignoring the particles surface properties. A more advanced numerical reaction rate model needs to be investigated to increase the simulation accuracy.

(4) In the current available experiments data, the first measurement point away from the wall is at r/R=0.949, but for CFB simulations, the numerical results show a very large gradient in the radial location between r/R=0.949 and 1 due to wall boundary conditions. Thus for both numerical and experimental methods, the flow in the region near the wall should be still investigated further.

Appendix

Agrawal (2001), who suggested using coarse meshes to solve gas-solids two-phase flow problems, indicated that the grid size within the order of 10-50 times of the particle diameter is ideal grid size. They also indicated that the grid size close to 10 times of particle diameter can be a critical value to make sure the numerical stability. In the Eulerian-Eulerian approach, the grid captures the particle cluster rather individual particles as demonstrated by Agrawal (2001) and Zhang et al (2001). This particle clusters is considered as a mesoscale structure arisen as a result of an instable motion between gas and particle phases, the length scale of which is about 10 times of the particle size. If the grid size is smaller than this length scale, the fluctuation will be revealed. Thus, the mesh independence study should be done with the mesh size not smaller than 10 times of the particle diameter.

For most simulations of gas-solids flow systems, the stability of the homogeneously fluidized state is corresponding to the traveling wavelength of the perturbations (Andrews IV, Loezos, and Sundaresan 2005). Generally, this length should be not smaller than 10 times of the particle diameter. Therefore, the selection of the minimum grid size should also follow this principle. Figure A shows the axial solids volume fraction distributions at the wall of the riser using different mesh sizes. The smaller size leads to more intensive fluctuation in the solids volume fraction at the wall.

Time step has a strong correlation with the mesh size for courant number in term of the numerical stability during the simulation. In this study, the time step is 10^{-4} s. However,

the time step independent results cannot be achieved. Figure B shows the radial solids volume fraction distribution at x=2.35m using different time steps. Even at time step of 10^{-6} s, the simulation result is still not independent of the time step, but the fluctuation in solids volume fraction is improved. Most difficultly, the current available performance of computer is 32 2.4GHz nodes. For the mesh no more than 20,000 grids, it will take about 2 weeks to simulate the case using 10^{-6} s time step. If increasing the mesh numbers, the computational cost would be as much as the single phase DNS method, which is too expensive to run. Thus, in consideration of accuracy and computational time, 10^{-4} s time step and the mesh with 12,093 cells are applied in this study.

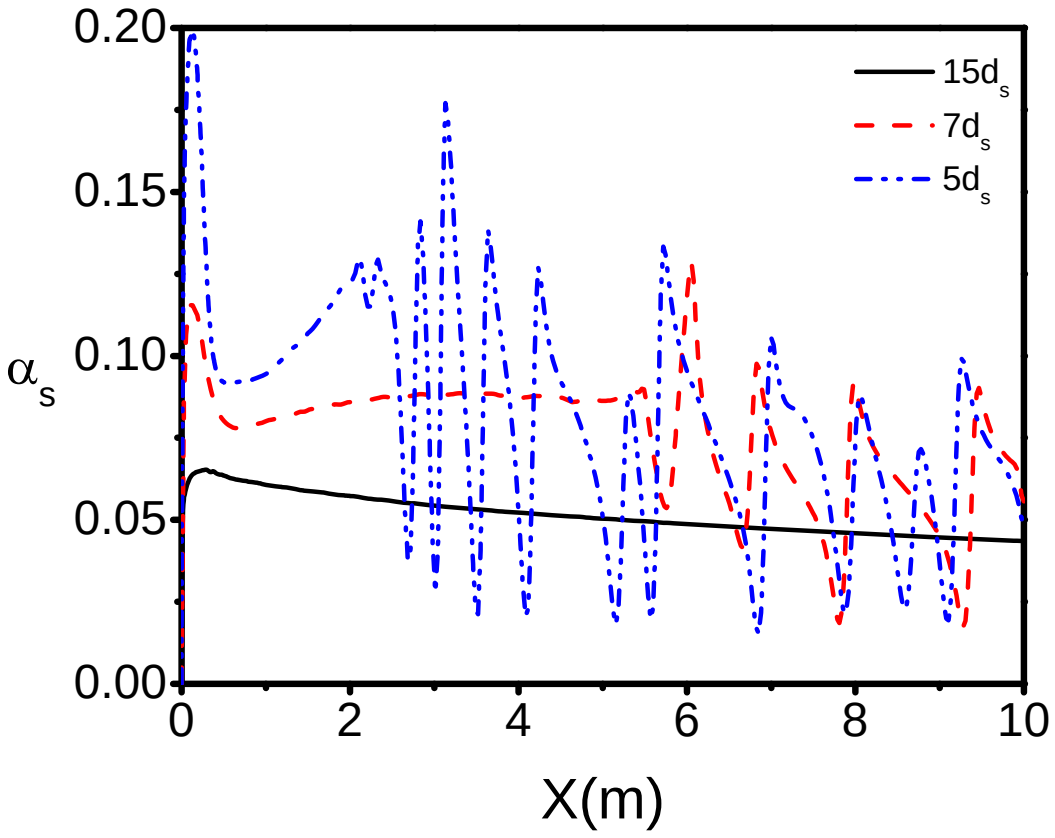

Figure A Solids volumes fraction distribution at the wall along the axial direction with different mesh sizes

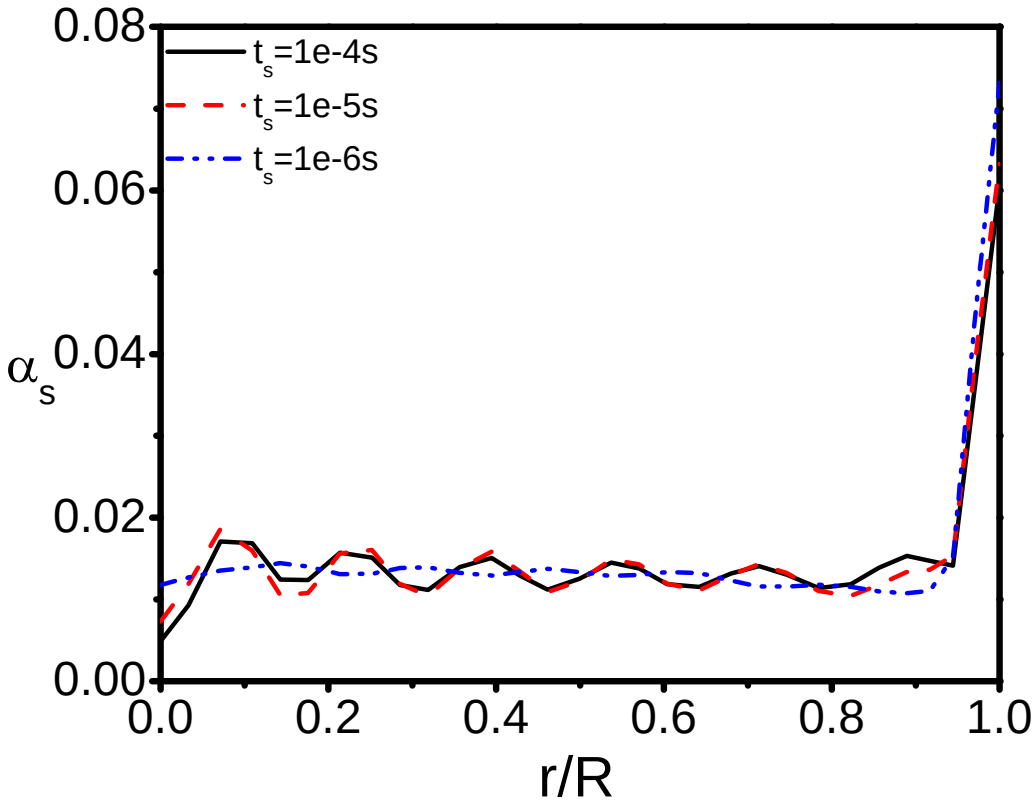

Figure B Solids volume fraction distribution in the radial direction using different time steps

Curriculum Vitae

Name:	Lei Kong
Post-secondary Education and Degrees:	Dalian University of Technology Dalian, Liaoning, China 2005-2009 Bachelor of Engineering
Honours and Awards:	Western Engineering Scholarship 2011-2012
Related Work Experience	Teaching Assistant The University of Western Ontario 2011